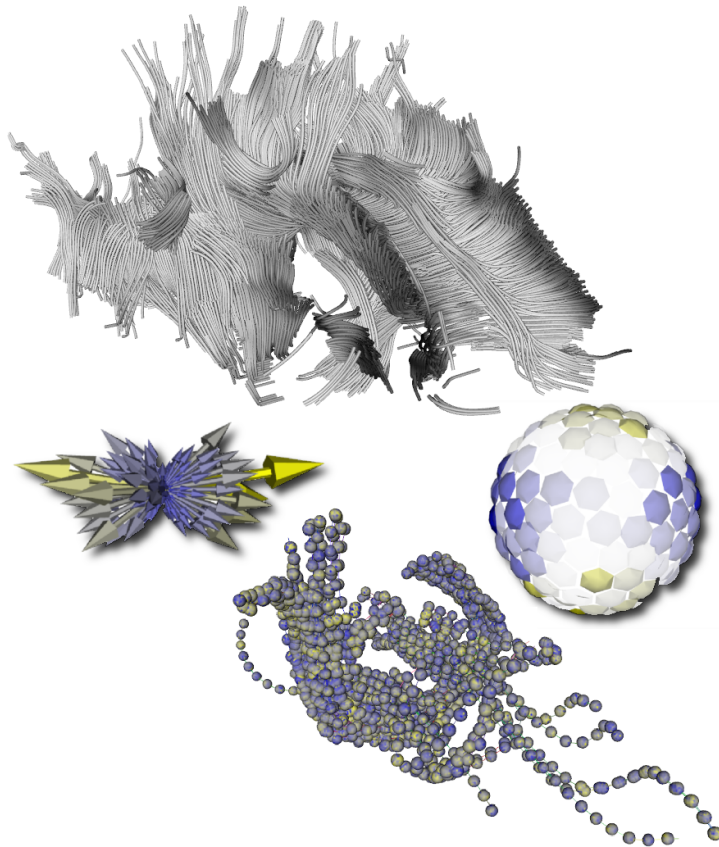


---

# Direct and Comparative Visualization Techniques for HARDI Data

---



RIK SONDERKAMP





DELFT UNIVERSITY OF TECHNOLOGY

FINAL THESIS

**Direct and Comparative Visualization  
Techniques for HARDI Data**

This final thesis is submitted in partial fulfillment of the requirements for the degree of master of science at the Delft University of Technology.

*Author:*  
Ing. Rik SONDERKAMP

*Thesis committee:*  
Prof. Dr. Ir. F.W. JANSEN  
Ir. F.H. POST  
Dr. C.P. BOTHA  
Dr. J.R. MILLES  
Dr. M.J.P. VAN OSCH

*Date:* September 30, 2010  
*Version:* Final (1.0)



## *Abstract*

DWI is an MRI imaging technique used to gain information concerning the diffusion process in tissue. Using DTI techniques, a diffusion profile can be constructed for fiber tract analysis. Recently developed HARDI techniques increase the detail to visualization on the process of diffusion. While HARDI reconstruction methods are used to model the underlying diffusion process, the HARDI signal attenuation data can be used for a better understanding of noise in DWI data.

This project addresses the direct visualization of HARDI data without any intermediate processing steps between acquisition and visualization. We present new glyph shapes for direct and comparative visualization of HARDI data using the signal attenuation or ADC and a multiple linked views layout. We developed new difference metrics to create a complete comparative visualization pipeline to identify and explore areas of interest.

Evaluation of our developed methods by means of a case study, indicates the techniques to be a valued addition. The comparative visualization allows for quick identification of areas of interest. The glyph representation allows for rapid exploration of local diffusion data.



## ACKNOWLEDGMENTS

From the Delft University of Technology, I would like to thank all people from the Computer Graphics group, in particular Charl Botha and Frits Post. Charl Botha was my direct supervisor during the project who always inspired me with innovative ideas on both the project and this thesis. Frits Post always kept the overview of this project and also provided valuable comments with reviews on this thesis.

I wish to thank Tim Peeters, Vesna Prčkovska, Paulo Rodrigues and Anna Vilanova Bartroli from the BioMedical Image Analysis group at the Eindhoven University of Technology. The use of their DTITool framework gave this project a flying start. I want to thank them for the help on the project and Vesna also for her advice on the parameters for the 7T MRI acquisition.

I wish to extend my thanks to our collaborators from the Leiden University Medical Center, specifically Julien Milles from the department of radiology and Thijs van Osch, Itamar Ronen and Andrew Webb from the C.J. Gorter center for high field MRI. I want to thank them for the many informal discussions which lead to inspiring and interesting ideas for this project and in particular Thijs for the custom 7T MRI acquisition.

Many thanks go out to my family and friends who have supported me throughout the project. Above all I want to thank my girlfriend, Corrine, who supported me during my thesis project and with whom I had a wonderful experience at the Nijmeegse vierdaagse.

Thank you.

Rik Sonderkamp, October 2010



# CONTENTS

- 1 Introduction** **1**
- 1.1 Research goals . . . . . 2
- 1.2 Contributions . . . . . 2
- 1.3 Thesis structure . . . . . 2
  
- 2 Background** **5**
- 2.1 Magnetic Resonance Imaging . . . . . 5
- 2.1.1 Scanner layout . . . . . 5
- 2.1.2 Resonance . . . . . 5
- 2.1.3 Spin relaxation . . . . . 6
- 2.2 Diffusion Weighted Imaging . . . . . 7
- 2.2.1 Principles . . . . . 7
- 2.2.2 Q-space acquisition . . . . . 8
- 2.2.3 Modeling diffusion . . . . . 8
- 2.2.4 Apparent Diffusion Coefficient . . . . . 9
- 2.3 DWI visualization . . . . . 9
- 2.3.1 Diffusion Tensor Imaging . . . . . 9
- 2.3.2 High Angular Resolution Diffusion Imaging . . . . . 10
- 2.3.3 Principal Component Analysis . . . . . 11
  
- 3 Methods** **13**
- 3.1 Direct HARDI visualization . . . . . 14
- 3.1.1 Direct glyph representations . . . . . 14
- 3.1.2 Color scales . . . . . 17
- 3.1.3 Anti-aliasing . . . . . 19
- 3.1.4 Signal normalization . . . . . 19
- 3.1.5 Glyph seeding . . . . . 20
- 3.2 Comparative visualization . . . . . 20
- 3.2.1 Difference metric . . . . . 20
- 3.2.2 Global difference visualization . . . . . 24
- 3.2.3 Comparative glyphs . . . . . 26
- 3.3 Multiple linked views . . . . . 29
- 3.3.1 Linked views . . . . . 29

## CONTENTS

3.3.2	Linked 3D cursor . . . . .	29
<b>4</b>	<b>Implementation</b>	<b>31</b>
4.1	Data formats . . . . .	31
4.2	Data conversion pipeline . . . . .	32
4.3	RFS Tools . . . . .	32
4.4	DTITool . . . . .	34
4.4.1	Run-time system . . . . .	35
4.4.2	GUI layout . . . . .	35
4.4.3	User interaction . . . . .	36
4.4.4	Rik tab . . . . .	36
4.5	DTITool implementation details . . . . .	37
4.5.1	Glyph shapes . . . . .	37
4.5.2	Multiple coupled views . . . . .	38
4.5.3	Slice viewer and gradient directions . . . . .	39
4.5.4	Comparative visualization . . . . .	39
4.5.5	PCA/FA difference metric . . . . .	39
4.5.6	ROI export function . . . . .	40
<b>5</b>	<b>Results</b>	<b>41</b>
5.1	Acquisition . . . . .	41
5.1.1	Scan setup . . . . .	41
5.1.2	Scan parameters . . . . .	41
5.2	Case study . . . . .	42
5.2.1	Introduction . . . . .	42
5.2.2	Case study definition . . . . .	42
5.2.3	Results . . . . .	43
5.2.4	Case study conclusions . . . . .	45
5.2.5	Improvements based on case study . . . . .	46
5.3	Data analysis . . . . .	48
5.3.1	Common data artifacts . . . . .	48
5.3.2	Observations in the data . . . . .	49
<b>6</b>	<b>Conclusion</b>	<b>55</b>
6.1	Conclusion . . . . .	55
6.2	Discussion . . . . .	56
6.3	Future work . . . . .	57
<b>A</b>	<b>Reconstruction methods</b>	<b>63</b>
A.1	Processing the signal . . . . .	63
A.1.1	Acquisition . . . . .	63
A.1.2	Relating signal to diffusion . . . . .	64
A.1.3	ODF . . . . .	64
A.2	Spherical Harmonics . . . . .	64
A.3	Reconstructing the PDF . . . . .	65
<b>B</b>	<b>DTITool mouse and key bindings</b>	<b>67</b>
<b>C</b>	<b>Export ROI file format</b>	<b>69</b>
	<b>Glossary</b>	<b>75</b>

## LIST OF FIGURES

2.1	Spinning and precession of protons . . . . .	6
2.2	Diffusion weighted spin echo scheme . . . . .	7
2.3	Conversion PDF to isosurface and ODF . . . . .	9
2.4	Barycentric space of anisotropies [KW99] . . . . .	10
2.5	Ellipsoid and superquadric tensor shapes . . . . .	11
2.6	Q-ball glyphs . . . . .	11
3.1	Implementation of our proposed framework . . . . .	13
3.2	Q-ball glyph . . . . .	14
3.3	Arrows glyph representation . . . . .	15
3.4	Spikes, cubes and spheres glyph representations . . . . .	16
3.5	The power crust surface reconstruction filter . . . . .	16
3.6	Comparison Q-ball glyph and power crust surface glyph . . . . .	17
3.7	Graph displaying composition of color scale and opacity . . . . .	18
3.8	Usage of color scales . . . . .	19
3.9	Color scale with single and double peak transparency option . . . . .	20
3.10	Anti-aliasing technique . . . . .	21
3.11	Fiber tract seeding for glyphs . . . . .	21
3.12	Difference metric slice views . . . . .	22
3.13	Decision tree for the PCA/FA difference metric . . . . .	23
3.14	Scalar range for the PCA/FA difference metric . . . . .	24
3.15	Isosurface visualization of difference metric . . . . .	25
3.16	Illustration showing the range and center parameters for the opacity function for the volume visualization . . . . .	25
3.17	Interactive modification of volume visualization . . . . .	26
3.18	Projected arrows representation . . . . .	27
3.19	Global trends in data using projected arrows representation . . . . .	27
3.20	The partial and colored spheres glyph representations . . . . .	28
3.21	Comparison between flat shading and Gouraud shading . . . . .	28
3.22	3D cursor . . . . .	29
3.23	Gradient direction selection over multiple voxels . . . . .	30
3.24	Gradient direction selection . . . . .	30

## LIST OF FIGURES

4.1	Conversion pipeline . . . . .	32
4.2	RFS ParRec2Nifti . . . . .	33
4.3	RFS NiftiVOIExtract . . . . .	33
4.4	RFS Nifti2Hardi . . . . .	34
4.5	RFS NiftiHeaderReader . . . . .	34
4.6	DTITool main window . . . . .	35
4.7	The Rik tab . . . . .	36
4.8	Multiple linked views VTK rendering pipeline . . . . .	38
5.1	Corpus Callosum showing motion artifact . . . . .	50
5.2	Motion artifact in forceps major . . . . .	50
5.3	Random noise in the Corpus Callosum area . . . . .	51
5.4	Random noise in single voxel in the Corpus Callosum area . . . . .	52
5.5	Artifact due to air cavities in the frontal area of the brain . . . . .	52
5.6	Noise at the boundary of the white matter . . . . .	53
6.1	Depth sort with transparent glyphs . . . . .	57
6.2	Fiber tracts from two tensor sets . . . . .	60
6.3	Classification pattern of a 90 degree rotation for a linearly anisotropic voxel . . . . .	61

LIST OF TABLES

2.1 First 8 folded icosahedra . . . . . 8

3.1 Number of colored arrows for arrows (PCA) representation . . . . . 15

4.1 Software libraries used for DTITool development . . . . . 35

4.2 Range specification for our implementation of the PCA/FA dif-  
ference metric . . . . . 39

4.3 Files generated with the ROI export function . . . . . 40

B.1 Mouse and keyboard combinations for moving the camera around  
in the visualization . . . . . 67

B.2 Existing and added key bindings in DTITool . . . . . 68

## LIST OF TABLES

# CHAPTER 1

## INTRODUCTION

Magnetic Resonance Imaging (MRI) is an imaging technique widely used today in clinical environments. MRI is often used for research purposes because no negative side effects are known for in-vivo scanning. This makes MRI for example suitable for studies to gain more insight in the working of the human body.

MRI includes a wide range of different acquisition techniques where each is specialized in acquiring specific characteristics of underlying tissue. One of these is Diffusion Weighted Imaging (DWI) which is specialized in measuring diffusion. Diffusion is of special interest in fibrous tissue such as the white matter of the brain. This makes DWI an ideal technique for brain image acquisition and research.

Early DWI techniques introduced an imaging technique called Diffusion Tensor Imaging (DTI). DTI fits the diffusion at a certain point in space to a tensor model. Three eigenvectors of the tensor are associated with the diffusion, the largest representing the principal direction of diffusion. The probability distribution is assumed Gaussian which prevents DTI to detect non-Gaussian features such as intravoxel fiber crossings. A solution was proposed by Tuch et al. in 1999 which was termed High Angular Resolution Diffusion Imaging (HARDI) [TWBW99]. HARDI does not fit the diffusion to a particular model which allows for the recognition of intravoxel features.

The tensor model is much appreciated in the field of DWI data visualization for its simplicity and versatility. Due to the assumption of Gaussian diffusion of the tensor model, each voxel is represented with three eigenvalues with corresponding eigenvectors. The simple nature of this model makes DTI popular in the visualization community. The limitation of three eigenvectors which is overcome by HARDI presents however new visualization possibilities.

HARDI data offers more detail but as it is a complex modality it requires special techniques to be processed. Reconstruction methods are needed to create a diffusion profile. Reconstructed data can then be used to represent the underlying diffusion process of a voxel. This can be done for example with interactive computer graphics applications. With the use of reconstruction methods, some data is lost in this transformation. When studying effects of noise in HARDI

data, it is also important to look at the non transformed data.

This project addresses the direct visualization of HARDI data without any intermediate processing steps between acquisition and visualization. We present new glyph shapes for direct and comparative visualization of HARDI data using the signal attenuation or ADC, a multiple linked views layout and a complete comparative visualization pipeline to identify and explore areas of interest.

## 1.1 Research goals

This project has two main research goals. The first goal is to allow exploration of HARDI data using novel low-level direct visualization methods. This allows researchers to have a closer look at the raw data without intermediate processing steps.

The second research goal is to give researchers more insight into noise artifacts of HARDI data and its causes. This is done by comparison of two acquisitions with equal scan parameters. Possible noise causes could be random noise, physiological noise, breathing or movement of the patient which may be classified as spatial-dependent, directional-dependent or time-dependent.

## 1.2 Contributions

We developed *techniques for the low-level visualization* and exploration of HARDI data. New glyph shapes are used to visualize local diffusion data. Implementation of a perceptually linear color scale allows the user to quickly identify the significant values of the data.

We developed new *comparative visualization techniques* for HARDI data. A complete pipeline allows for the identification of areas with large differences, zooming into the data and exploring the data on local scale. We present new difference metrics used to quantify the difference between voxels. These metrics are then used in a slice viewer and volume visualization to allow the user to identify areas of interest. A ROI can then be created which allows for local data exploration.

We have created a *prototype implementation* of the techniques mentioned above in a multiple coupled views layout. We also created a conversion pipeline to convert data from the MRI scanner format to the format of our application framework.

As part of the *evaluation of our proposed techniques*, we performed a case study with MRI physicists. Results from this case study as well as comments and suggestions from informal meetings are used to improve on the effectiveness during development of our proposed techniques.

The contributions mentioned in this section will be further elaborated on in chapter 3. The evaluation is discussed in chapter 5.

## 1.3 Thesis structure

The rest of this thesis contains the following chapters. Chapter 2 gives an introduction to MRI and DWI. Physical principles are discussed as well as details on acquisition and further processing of the data for visualization purposes.

Chapters 3 and 4 explain the techniques developed and implemented. Chapter 3 elaborates on all contributions mentioned in section 1.2. All developed techniques will be discussed together with explanations on their advantages and disadvantages. The more technical details on the implementation will be explained in chapter 4.

The results will be covered in chapter 5. First a description will be given of the MRI scans performed for evaluation of our developed techniques. Then results of a case study will be discussed which we performed as part of the evaluation of our developed techniques. We will also present some observations from exploration of the data using our visualization techniques.

Conclusions together with a discussion will be presented in chapter 6. The chapter concludes with future research topics which we think could contribute to direct and comparative HARDI visualization in the future.

## Chapter 1. Introduction

## CHAPTER 2

## BACKGROUND

This chapter provides background information on the principles of Magnetic Resonance Imaging (MRI) and Diffusion Weighted Imaging (DWI). The data can be used for a wide range of visualization applications, both 2D and 3D. Several processing and visualization techniques are discussed for the DWI data modality.

### 2.1 Magnetic Resonance Imaging

Magnetic Resonance Imaging (MRI) is a well known imaging technique used for non-invasive image acquisition. MRI allows for acquisition of data revealing in-vivo information of tissue. This section will discuss the scanner layout and physical principles of MRI.

#### 2.1.1 Scanner layout

The main feature of an MRI scanner is the magnet which generates a strong magnetic field. This field is usually 1.5 or 3 Tesla though experimental uses go to 7 Tesla for whole body scanners. Much larger values beyond 7 Tesla can be found for non-human scanning.

For comparison, one Tesla equals 10,000 Gauss. While the earth's magnetic field ranges from 0.3 to 0.6 gauss, a MRI scanner exceeds the earth's magnetic field significantly.

Other important components are the gradient magnets. These are used to make local changes to the magnetic field. Next to that is the RF pulse emitter which is used to induce resonance and change the angle of the spin axis. These components will be explained in more detail in the following sections. Acquisition is normally done using a regular grid of voxels.

#### 2.1.2 Resonance

The concept of MRI starts with protons which are sub-atomic parts of hydrogen atoms. The protons are spinning around an axis (also called the spin axis). If

the protons are subjected to a magnetic field where the spin axis is not co-axial to the axis of the magnetic field, the spin axis starts to rotate. This is a principle known as precession. Influencing the spin precession and measuring the effects form the fundamentals of MRI [HJM<sup>+</sup>06, Bam03, Poo05].

In general, all protons have a random orientation and so the axis of precession is random (figure 2.1 (a)). To take advantage of spin precession, first the protons are subjected to a strong magnetic field (figure 2.1 (b)). When the protons are

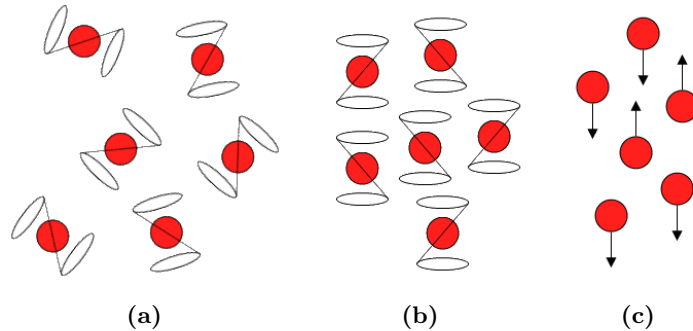


**Figure 2.1:** Spinning and precession of protons. (a) shows the protons with random spin precession axis orientation. (b) shows the same protons aligned due to the influence of a large magnetic field. (c) shows the magnetization for the protons when subjected to the large magnetic field.

placed in this strong magnetic field, the spin axes are aligned with the magnetic field, some align with the magnetic field and some in opposite direction (figure 2.1 (c)). When considering that there are millions of protons, there is a net magnetization. This net magnetization is then used in measurements of the object being scanned.

For the precession to become visible, the spin axis must be tilted away from the co-axial orientation to the magnetic field. To achieve this, an angular momentum can be excited on the protons. The protons have a certain frequency at which the spins precess, also known as the Larmor frequency. This frequency  $\omega$  is given by

$$\omega = \gamma B_0 \quad (2.1)$$

where  $\gamma$  is the gyromagnetic ratio and  $B_0$  the magnitude of the magnetic field. Using a Radio Frequency (RF) pulse, this angular momentum is excited on the protons and the direction of the axis of precession can be changed. This is done by setting the RF to the Larmor frequency which induces resonance on the protons rotating the axis of precession.

### 2.1.3 Spin relaxation

The RF pulse is used to influence the axis of precession. When the excitation of the RF pulse on the protons ends, the axis will return to the equilibrium state co-axial to the magnetic field axis. This principle is known as spin relaxation. The relaxation  $T_1$  time and  $T_2$  time combined with the proton density influence the signal measured by the MRI scanner which represent characteristics of the tissue.

The proton density is the number of protons in a voxel. The  $T_1$  time indicates the time it requires for the protons to return to their equilibrium state. The  $T_2$  time indicates the time after which the MRI signal has faded after excitation.

## 2.2 Diffusion Weighted Imaging

Diffusion Weighted Imaging (DWI) is a specialized MRI technique with specific parameters for the MRI scanner. With DWI, diffusion weighted images are acquired which describe the diffusion of water molecules in tissue. In particular, research to fibrous tissue benefit from DWI. As a large part of the brain consists of fiber tracts, the white matter, this can be studied in more detail using DWI [HJM<sup>+</sup>06]. This section gives a introduction to DWI. More details and mathematical background is provided in appendix A.

### 2.2.1 Principles

For DWI acquisitions, the spin echo sequence is usually used to obtain a signal from the MRI scanner [Bam03, HJM<sup>+</sup>06]. The acquisition scheme is shown in figure 2.2.

Diffusion-encoding gradients are used to generate magnetic field gradient which changes the phase of the protons. The diffusion-encoding gradients are used twice, one time before the 180 degree RF pulse and one time after the 180 degree RF pulse. The effect is that with the first pulse the phase is changed. The second pulse changes the phase back to normal canceling the first one out. When the particle has moved however, the second pulse does not counteract the first phase shift completely resulting in a total phase shift. In the end this results in a signal attenuation measured by the MRI scanner which indicates diffusion.

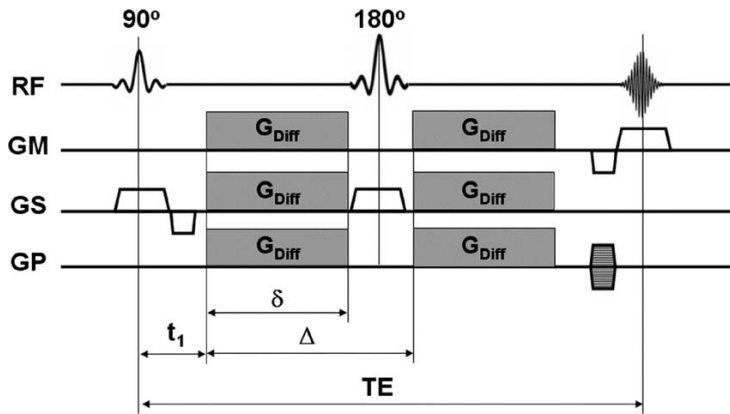


**Figure 2.2:** Diffusion weighted spin echo scheme. TE=Time Echo,  $\mathbf{G}_{\text{diff}}$ ,  $\delta$  and  $\Delta$  are the strength, duration and space of the applied gradient of each TE/2 period respectively. GM, GS and GP are the readout direction, phase-encoding direction and section selection direction respectively. [Image courtesy of [Bam03]]

The strength of the diffusion sensitizing gradient is defined as the  $b$ -value. A  $B_0$  image is referred to as a image with a  $b = 0$  value. This is often used as

reference for images with  $b \neq 0$ . The direction in which diffusion is measured is said to be the gradient direction. Measuring multiple directions allows for the reconstruction of a diffusion profile.

### 2.2.2 Q-space acquisition

Q-space is defined as a 3D space where vectors from the origin describe the gradient direction by the vector's orientation and  $b$ -value by the vector's length. This makes the origin a  $B_0$  measured image while for each other vector a gradient direction is measured with a certain  $b$ -value. An optimal distribution scheme for acquisition would be to use multiple  $b$ -values in evenly distributed directions. From a study by Kuo et al. in 2005, it showed that using 515 measurements results in the optimal acquisition scheme [KWW<sup>+</sup>05]. This process provides detailed information but is time consuming.

An alternative is to use vectors which are all of the same length, hence where the  $b$ -value is constant. This is also known as Q-ball imaging [TRW03]. With a certain number of measurements, it is important that all are evenly distributed over the sphere. This can be done using a folded icosahedron gradient encoding scheme.

The icosahedron is the largest 3D polyhedron shape with equal triangles. With the folded icosahedron gradient distribution encoding scheme, the triangles are subdivided by a number of  $N$ . The icosahedron is then said to be a  $N$  folded icosahedron. For Q-space acquisitions, the vertices are used to determine the gradient directions. The number of directions  $D$  derived from  $N$  is described with the following relation:

$$D = 10N^2 + 2 \quad (2.2)$$

The first few folded icosahedra are displayed in table 2.1.

N	1	2	3	4	5	6	7	8
D	12	42	92	162	252	362	492	642

**Table 2.1:** The number of polygons for the first 8 folded icosahedra

### 2.2.3 Modeling diffusion

The data from acquisition can be used to model the underlying diffusion. A 3D probability space can be reconstructed which defines the probability of diffusion. To build a 3D probability space, reconstruction methods can be used which are often associated with Fourier transformations. Though reconstruction methods go beyond the scope of this thesis, a short introduction is given in Appendix A.

The resulting 3D function is known as a *Probability Density Function* (PDF), sometimes also called the (3D) displacement distribution. It describes a 3D space where each point represents the probability that a particle starting at the origin will end up at that location. An example of a PDF is shown in figure 2.3.

As a 3D space, the PDF is still quite complex and needs to be reduced. A straightforward way is to use an isosurface. This method is however more

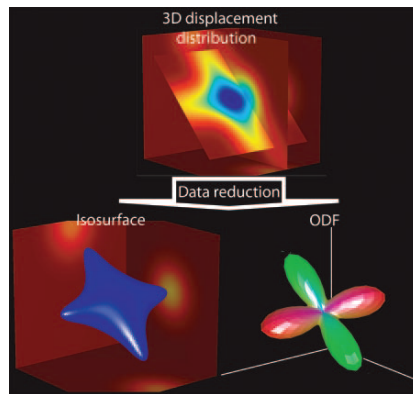


**Figure 2.3:** Conversion of a PDF to isosurface and ODF. [Image courtesy of [HJM<sup>+</sup>06]]

sensitive to noise as only part of the data is used. A more commonly used method is to convert the PDF to an *Orientation Distribution Function* (ODF). The ODF can be considered a deformed sphere which is a radial projection of the PDF. For each value of the ODF, the value is a summation of the values of the PDF in the same direction. An example of an isosurface and (min/max normalized) ODF is displayed in figure 2.3.

### 2.2.4 Apparent Diffusion Coefficient

The diffusion for a single direction can be described by the Apparent Diffusion Coefficient (ADC). The ADC is defined as

$$ADC = -\frac{1}{b} \ln \frac{S_n}{S_0} \quad (2.3)$$

where  $b$  is the  $b$ -value used for the measurement and  $S_n$  and  $S_0$  are the measured signal and signal of the unweighted image respectively [Bam03]. This relation provides a transformation from the measured signal attenuation to values representing the diffusion.

## 2.3 DWI visualization

DWI visualization techniques can be divided into 2 distinct groups. The first is glyph visualization where each voxel is represented as a glyph displaying local diffusion information. The second technique tries to virtually reconstruct and visualize fiber bundles. This is also known as tractography and displays the global structural connectivity.

### 2.3.1 Diffusion Tensor Imaging

DTI is a popular visualization method for DWI data. The technique requires a minimum of six different gradient directions and a  $B_0$  image to be acquired. For each voxel, the data is fitted to a tensor which is a  $3 \times 3$  symmetric positive

definite matrix. From this tensor, three eigenvalues with corresponding eigenvectors can be determined which indicate the diffusion. Early visualizations use spheres deformed by the eigenvectors of the tensor to create ellipsoids as glyph shapes.

A classification of diffusion was presented in 1997 by Westin et al. These are linear, planar and spherical which are indicated by  $c_l$ ,  $c_p$  and  $c_s$  respectively [WPG<sup>+</sup>97]. These are defined as:

$$\begin{aligned} c_l &= \frac{\lambda_1 - \lambda_2}{\lambda_1 + \lambda_2 + \lambda_3} \\ c_p &= \frac{2(\lambda_2 - \lambda_3)}{\lambda_1 + \lambda_2 + \lambda_3} \\ c_s &= \frac{3\lambda_3}{\lambda_1 + \lambda_2 + \lambda_3} \end{aligned} \quad (2.4)$$

$\lambda_i$  define the three eigenvectors with  $\lambda_1 \geq \lambda_2 \geq \lambda_3$ . Figure 2.4 displays the barycentric space of anisotropies.

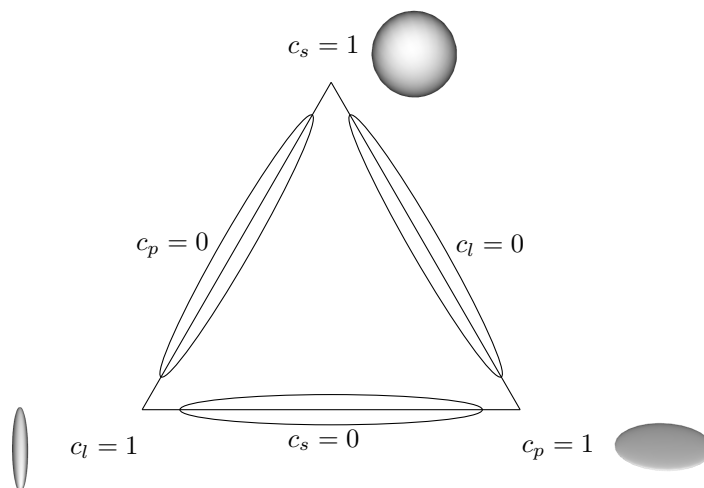


**Figure 2.4:** Barycentric space of anisotropies [KW99]

One of the improvements on the ellipsoid shapes was proposed by Kindlmann in 2004. The proposed superquadric shapes were developed in an attempt to decrease the ambiguous nature of ellipsoids [Kin04]. An example of ellipsoids and superquadric shapes is shown in figure 2.5 which clearly shows the decrease of ambiguity when using superquadric shapes.

With some visualizations there is the need for a single scalar value defining the degree of anisotropy of a voxel. The Fractional Anisotropy (FA) is a well known metric based on the eigenvalues and is widely used for visualization purposes. The scalar output of the FA is a number between 0 and 1, 0 representing perfect isotropy and 1 representing perfect anisotropy.

### 2.3.2 High Angular Resolution Diffusion Imaging

HARDI techniques have been introduced to overcome some limitations of the DTI tensor model. DTI has a maximum of three directions of diffusion which ex-

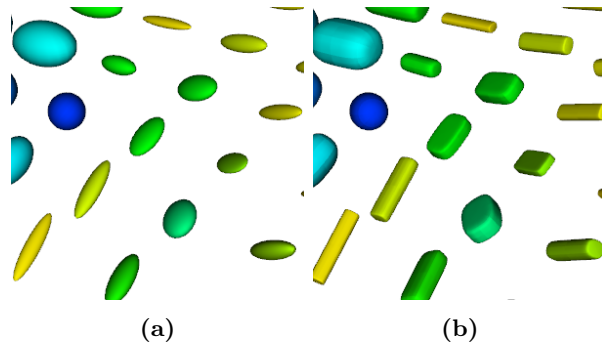


**Figure 2.5:** Ellipsoid (a) and superquadric (b) tensor shapes.

cluded the modeling and visualization of intravoxel white matter fiber crossings. With HARDI, a far greater number of diffusion directions is measured (typically  $n > 60$ ). This results in a more complex model though able to present more details of the underlying diffusion process.

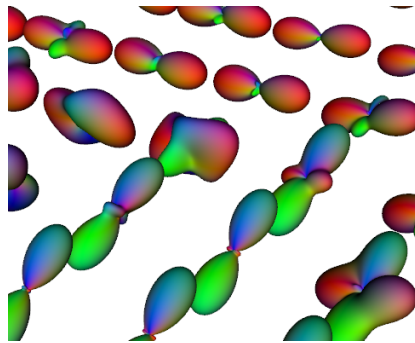


**Figure 2.6:** Q-ball glyphs showing spheres deformed by Q-ball reconstructed ODFs.

With the introduction of HARDI imaging, new glyph types had to be used to show the details enclosed by the modality. One of these methods is to use a sphere and deform it according to the ODF of the voxel. An example of this visualization method is shown in figure 2.6. Peeters et al. have implemented a GPU ray casting technique in 2009 [PPvA<sup>+</sup>09] which allows the deformed sphere shapes to be rendered using the GPU. This made it possible to explore large parts of HARDI data (i.e. full slice) at interactive frame rates.

### 2.3.3 Principal Component Analysis

The number of measurements for a HARDI dataset sometimes requires the data to be reduced. Principal Component Analysis (PCA) is a data reduction technique to compute the main trend of many data points. PCA can be utilized with HARDI data to compute the principal diffusion components.

To use PCA for HARDI data, first a set of vectors is created from the gradient directions multiplied by their associated signal attenuations. Then a

## Chapter 2. Background

$3 \times 3$  covariance matrix is created with these vectors. This matrix is then used for eigenanalysis which results in the eigenvalues and eigenvectors of the matrix [Smi02].

# CHAPTER 3

---

## METHODS

For the direct visualization of HARDI data, we developed a framework that combines low-level visualization techniques in a multiple linked views setup. We developed a complete comparative visualization pipeline with techniques for global and local data exploration. We developed difference metrics for global difference exploration. Furthermore we developed new low-level glyphs for local data exploration including glyphs specific to comparative visualization. Figure 3.1 shows the implementation of our developed framework.

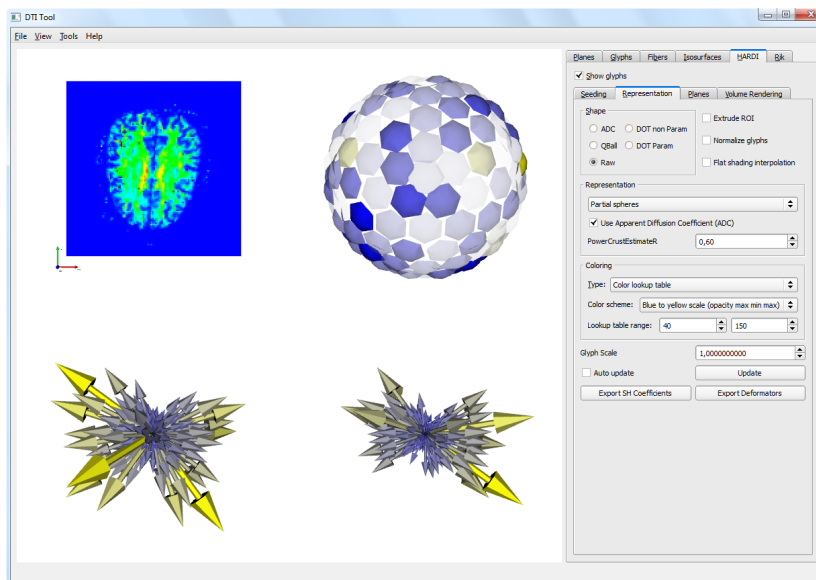


**Figure 3.1:** Implementation of our proposed framework.

This chapter will elaborate on the techniques we developed in an effort to answer the research goals described in section 1.1. The direct glyph representations will be discussed first, followed by the multiple views layout. The chapter then concludes with comparative visualization techniques.

### 3.1 Direct HARDI visualization

Deformed spheres are often used for glyph visualization of HARDI data. This is done by deforming a sphere with unit radius, for example according to the ODF of the qball reconstruction method as shown in figure 3.2. This visualization method gives comprehensive information about the diffusion which can be used to derive information concerning the underlying fibers. Figure 3.2 shows a cross-like glyph shape possibly because of two intersecting fiber tracts.

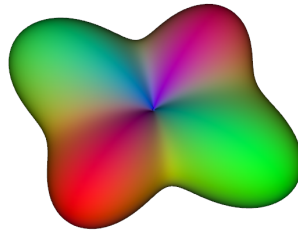


**Figure 3.2:** Q-ball glyph using 4<sup>th</sup>-order qball reconstruction.

One of the research goals of this project is to get more insight into the measured signal attenuation. For each voxel, a signal attenuation is measured by the scanner for all gradient directions. When the data is transformed using reconstruction methods, most of the signal attenuation data is lost in the process.

We developed new glyph representations to represent the signal attenuation. There are two options for the values to use in the visualization. The first is to use the measured signal attenuation directly. While these values do not represent the diffusion (see section 2.2.1), a second option uses the ADC (see section 2.2.4) as values for the glyph. This makes the glyph represent the actual diffusion.

#### 3.1.1 Direct glyph representations

This section will explain all the developed glyph representations for single dataset HARDI data. Details are explained as well as advantages and disadvantages for each of the glyphs.

##### Arrows representation

The first method developed is a glyph shape where each gradient direction is represented with an arrow. Each arrow points in the gradient direction and is scaled to the signal attenuation or ADC. When the ADC is used, the resulting glyph reflects the ODF of the voxel. The first arrows representation, also called original arrows representation (see figure 3.3(a)), was shown at a meeting with MRI physicists (19-02-2010) where it was well received.

We developed a second arrows representation (see figure 3.3(b)) with thinner arrows. The new representation appears more cluttered increasing visual

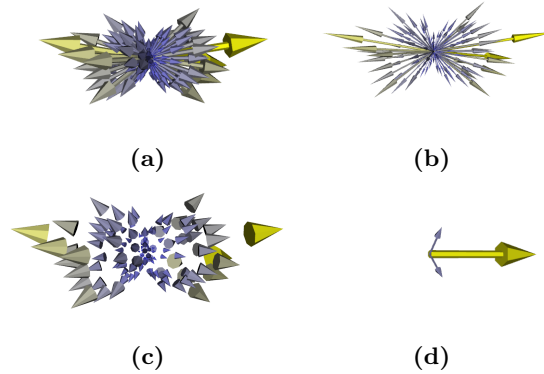


**Figure 3.3:** (a) original and (b) new arrows glyph representation of signal attenuation. (c) cones representation and (d) arrows representation of PCA analysis.

complexity but occlusion is decreased as more directions are visible. We also developed a representation with only the arrow heads: the cones representation. This representation decreases the cluttering as the arrow shafts are not rendered (see figure 3.3 (c)).

The arrows PCA representation consists of three arrows representing the eigenvectors resulting from PCA analysis of a voxel (see section 2.3.3). The arrows representation using PCA is shown in figure 3.3 (d). The largest eigenvalue(s) is/are colored yellow which is determined according to the definition in table 3.1. Other arrows are colored gray.

eigenvalues	# of yellow arrows	Anisotropy
$\lambda_1 \gg \lambda_2 > \lambda_3$	1	linear anisotropy
$\lambda_1 > \lambda_2 \gg \lambda_3$	2	planar anisotropy
$\lambda_1 > \lambda_2 > \lambda_3$	3	spherical anisotropy

**Table 3.1:** Number of colored arrows for arrows (PCA) representation.  $\lambda_i$  indicates the eigenvectors with  $\lambda_1 > \lambda_2 > \lambda_3$ .

### Spikes and cubes

We developed the spikes and cubes representations to decrease cluttering and increase information value of the visualization as opposed to the arrows representation. The spikes and cubes representations are shown in figure 3.4 (a) & (b). The spikes representation increases performance and decreases visual complexity. Due to the small tip of each spike however, there is not a clear definition of the signal attenuation or ADC.

The cubes representation also reduces occlusion though there is an increased visual complexity. Also due to a rather undefined origin, the 3D perspective is not always clear. Due to increased performance, the spikes representation is useful for large ROIs while the cubes representation is most useful when considering a limited number of glyphs.

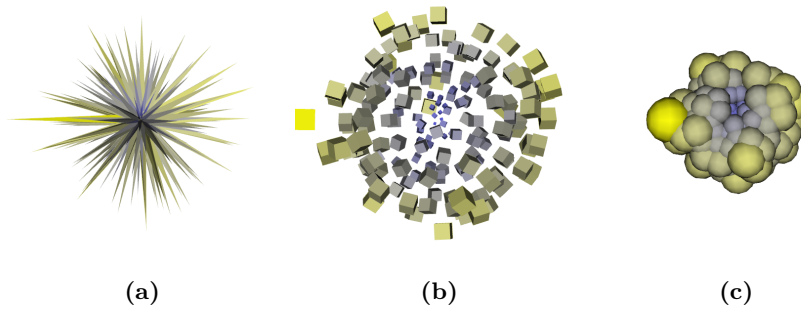


**Figure 3.4:** Spikes (a), cubes (b) and spheres (c) glyph representations.

### Spheres

The spheres representation presents all gradient directions with spheres. This created a blob-like form which, when using the ADC, represents the diffusion. Therefore this representation appears as a higher level representation of the diffusion of a voxel while maintaining the flexibility to explore individual gradient directions. The sphere representation is shown in figure 3.4 (c).

The spheres representation reduces visual complexity but occlusion is increasing as some spheres are small and are behind or inside other spheres. This is often not a problem because the smaller values are not significant and also because the glyph reflects a high-level description of the diffusion.

### Surface reconstruction & dots

Creating representations as discussed in the previous sections can be beneficial for direct HARDI data exploration. It is also useful to have a bridge between these low-level representations and the reconstructed representations modeling the ODF of a voxel. Therefore we developed a glyph representation which uses a surface reconstruction to reflect the diffusion profile. The signal's ADC is used in order to reflect the ODF.

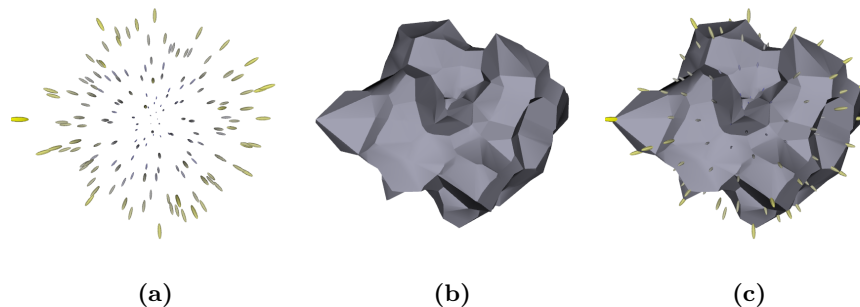


**Figure 3.5:** The power crust surface reconstruction filter. (a) Dots representing the signal attenuation. (b) The power crust surface reconstruction. (c) Combined power crust surface reconstruction and dots signal attenuation.

For generation of a surface based on the ADC values of the glyph, we utilized

the power crust algorithm developed by Amenta et al. [ACK01]. The algorithm was made available to VTK by Jim Hutton [Hut]. The power crust surface reconstruction algorithm creates closed 3D surface(s) from a number of points.

The power crust surface reconstruction sometimes gives unexpected results. This is because of the relatively sparse distribution of points and the relative large distances between these points and/or outliers of the data points. Therefore the surface sometimes contains holes or multiple surfaces are created for a single voxel.

This can partially be solved by altering the `estimate_r` parameter for the power crust algorithm. Altering the default value of 0.6 sometimes improves output of the algorithm. The optimal setting for this parameter is dependent on the glyph(s) in the ROI. Therefore the `estimate_r` parameter is user-configurable in our framework.

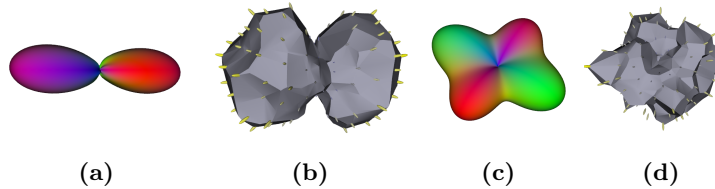


**Figure 3.6:** (a) Q-ball representation and (b) power crust surface of high anisotropy voxel. (c) Q-ball representation and (d) power crust surface of planar anisotropy voxel.

We developed three representations for surface reconstruction of the diffusion data: dots, power crust and power crust with dots. The dots representation (figure 3.5 (a)) shows small ellipsoids which appear as dots to represent the diffusion measurements. The second is a power crust surface reconstruction (figure 3.5 (b)) using the signal attenuation or the ADC values. The third representation combines the first two representations (figure 3.5 (c)) to allow the user to link the diffusion measurements with the resulting surface reconstruction.

Our observation was that the shape of the power crust surface reconstruction glyph reflects the shape of the reconstructed glyph. As an example, figures 3.6 (a) & (b) show a linearly anisotropic voxel with q-ball and power crust surface representations respectively. The representations clearly shows a high probability for the diffusion going from left to right.

When the voxel is planar or spherically anisotropic however, the shape of the power crust surface does not give an accurate reflection of the reconstructed glyph. This is because of the relative sparse distribution of measurements which serve as input for the power crust algorithm. An example of planar anisotropy is shown in figure 3.6 (c) & (d). The power crust glyph representation can be advantageous to use when comparing the ODF shape with the actual measurements. For this purpose, the dots can be used to explore the influence of individual measurements to the diffusion profile.

### 3.1.2 Color scales

Coloring the glyph representations is an effective way to emphasize the meaning of the data. We used several color scales to color the glyphs which are based on the perceptually linear color scale developed by Haim Levkowitz [LH92]. We

## Chapter 3. Methods

included two options for use of transparency and an option to use significance thresholding. The range of the color scales can be modified interactively to influence the contrast of the color scale for the selected ROI.

The blue to yellow color scale, shown in figure 3.8 (a), is used to indicate low to high values respectively. We added two alternatives for the transparency, single peak and double peak (see figure 3.7). Both scales are used to make insignificant values transparent.

The single opacity peak color scale can be used for the direct glyphs (section 3.1.1) to emphasize the highest values. The double opacity peak color scale can be used for the comparative glyphs (section 3.2.3) to emphasize highest and lowest differences.

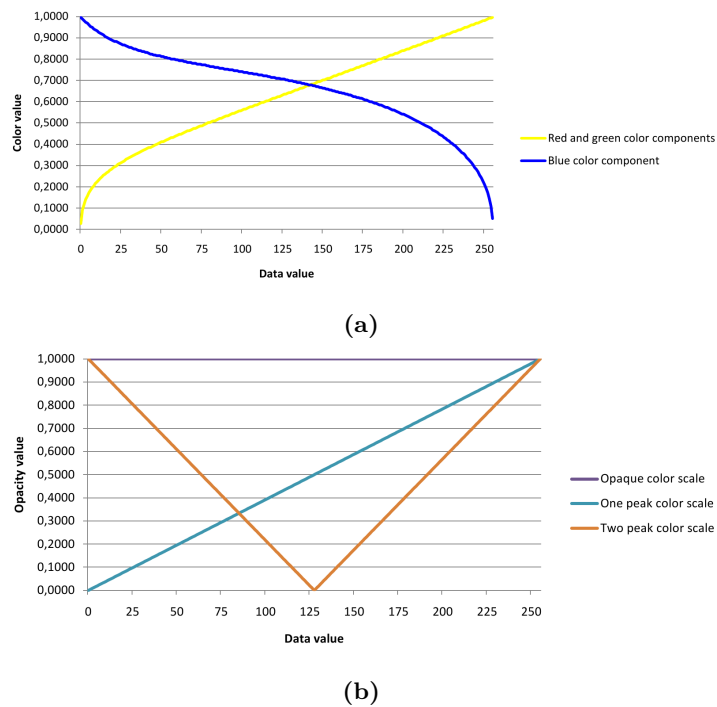


**Figure 3.7:** Graph (a) shows the color components for the lookup table for the color scales. For a certain input value, the red, green and blue components are displayed. The red and green components are combined (yellow) because they have the same values. (b) shows the composition of the transparency for all color scales.

For significance thresholding, user configurable upper and lower thresholds determine the significant values of the measurements. These are then colored blue and yellow for low and high values respectively. All values in between are colored gray and made transparent which allows for fast recognition of the extreme values of a voxel. An example is shown in figure 3.8 (b).

Graph 3.7 (a) shows the composition of the colors (RGB) for the perceptually linear color scale. Graph 3.7 (b) shows the composition of the transparency value for all color scales. Figure 3.9 shows examples of the color scales using a single and double opacity peak.

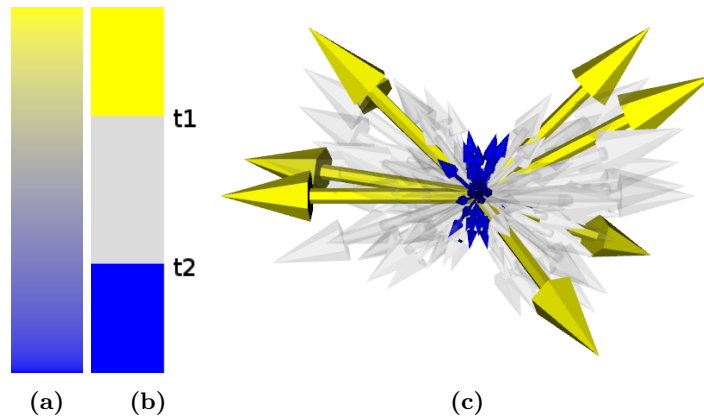


**Figure 3.8:** (a) Perceptually linear blue to yellow color scale. (b) shows the color scale with significance thresholding,  $t_1$  and  $t_2$  indicate the upper and lower threshold. (c) shows coloring of glyph with significance thresholding showing top 20% and lower 40% of the glyph's signal attenuation values in yellow and blue respectively.

### 3.1.3 Anti-aliasing

Aliasing is a recurrent problem in computer graphics. Aliasing is an effect where the image is distorted, often because of insufficient pixels used to display a high(er) resolution image or model. This results in unwanted artifacts in the final image. One of the artifacts is that pixels can be seen at sharp edges of objects where they do not form a smooth line but rather create a jagged line. The effect is often called a staircase effect. With anti-aliasing techniques however, aliasing artifacts such as the staircase effect can be reduced.

The staircase effect increases the visual complexity in our visualization. Therefore we used anti-aliasing to reduce this effect and also decrease the visual complexity. Figure 3.10 (a) shows an arrow representation without anti-aliasing where the staircase effect can be clearly seen in the enlarged arrow. Figure 3.10 (b) uses anti-aliasing to smoothen out the staircase resulting in a smoother edge of the arrow.

### 3.1.4 Signal normalization

Normalization is necessary for correct interpretation of the signal values. Normalization over the whole dataset enables inter-voxel comparison. This however limits the exploration of single voxels which have a small range of signal attenuation or ADC values.

A user configurable option allows for two normalization options. The first is normalization over the whole dataset which enables comparison of all glyphs in the ROI. The second is normalization per glyph which enables improved exploration for single glyphs and enables improved identification of the diffusion profile.

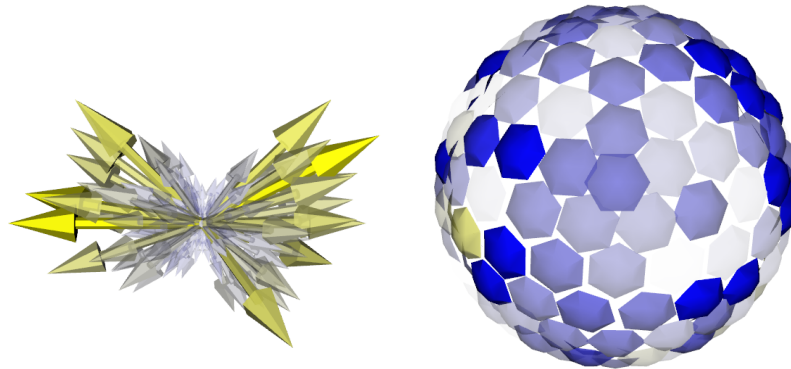


**Figure 3.9:** Color scale with single and double peak transparency option. (a) shows arrows representation for a single dataset. (b) shows partial spheres representation showing the difference between two datasets.

### 3.1.5 Glyph seeding

Defining the area for which to generate glyphs, also referred to as seeding, can be done in two ways. The first is based on a user drawn 2D ROI in the 2D slice viewer. The second method is to seed glyphs according to tractography results based on the tensor dataset. This allows for the exploration of differences along fiber tracts. An example of this technique is shown in figure 3.11.

## 3.2 Comparative visualization

To allow exploration of differences between HARDI datasets, we developed new difference metrics. The difference metrics indicate the difference between voxels using a scalar value. These metrics can then be used in the slice view, volume visualization or isosurface visualization. We also developed three glyph shapes to display differences at glyph level.

### 3.2.1 Difference metric

We developed six difference metrics. Each difference metric obtains a scalar value for the difference of two voxels. The difference metrics developed are the difference and normalized difference, ADC and normalized ADC, PCA and

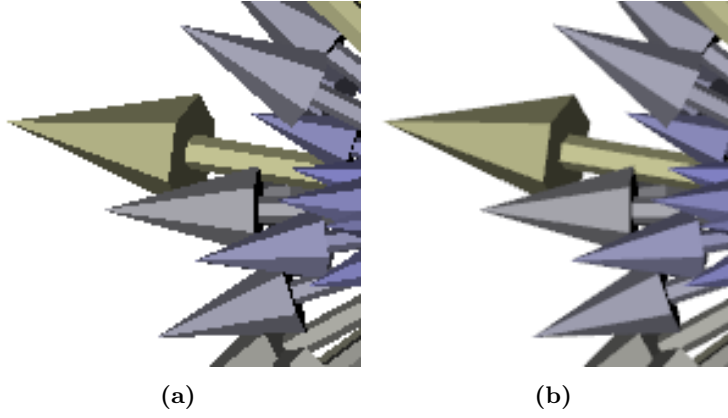


**Figure 3.10:** Arrows representation showing aliasing effects (a). (b) shows the arrows representation using anti-aliasing.

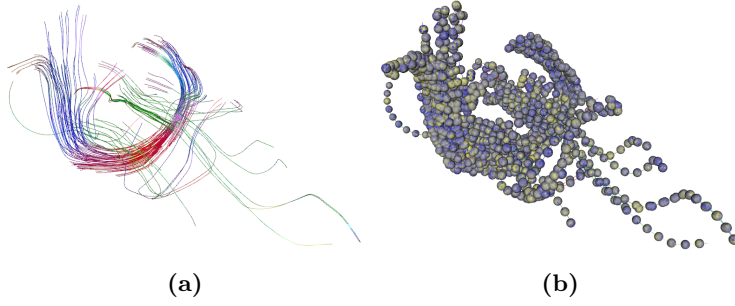


**Figure 3.11:** Fiber tracts used as seeding for the glyphs. (a) shows the fiber tracts derived from the tensor dataset and (b) shows colored spheres using the fiber tracts as seeding.

PCA/FA metrics. Equation 3.1 shows the equations associated with each metric.

$$\text{Difference} : \sum_{n=1}^N |a_i - b_i| \quad (3.1a)$$

$$\text{Normalized difference} : \sum_{n=1}^N \frac{|a_i - b_i|}{|a_i| + |b_i|} \quad (3.1b)$$

$$\text{ADC difference} : \sum_{n=1}^N |ADC(a_i) - ADC(b_i)| \quad (3.1c)$$

$$\text{Normalized ADC difference} : \sum_{n=1}^N \frac{|ADC(a_i) - ADC(b_i)|}{|ADC(a_i)| + |ADC(b_i)|} \quad (3.1d)$$

$$\text{PCA} : 1 - \text{abs}(\overline{ev_a} \cdot \overline{ev_b}) \quad (3.1e)$$

Here,  $a$  and  $b$  denote the two datasets,  $N$  the number of gradients and  $ev_a$  and  $ev_b$  denote the principal eigenvector of dataset  $a$  and  $b$  respectively. Figure

3.12 shows a slice view with each of the difference metrics. Details for each metric will now be discussed.

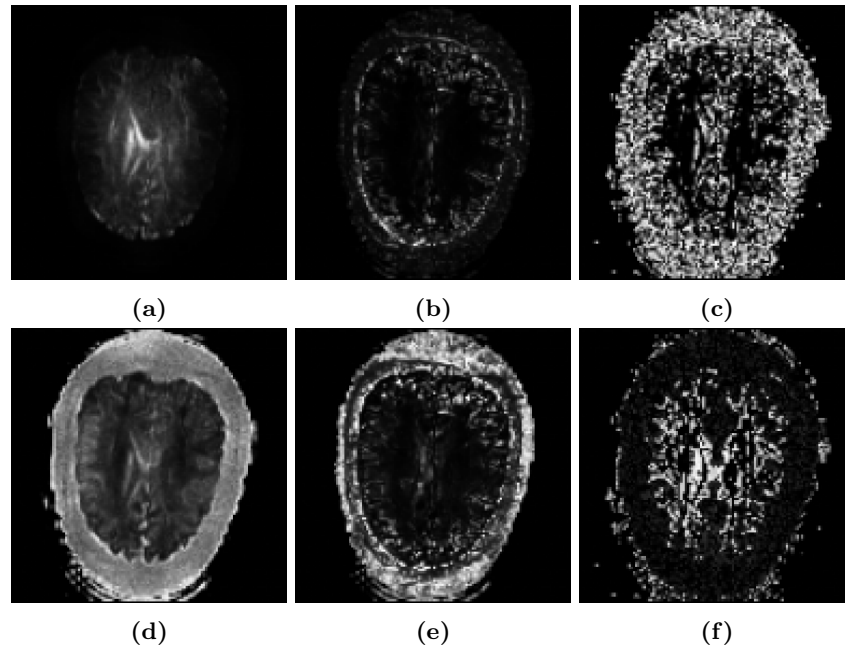


**Figure 3.12:** Difference metric slice views. The slice views show the (a) signal difference, (b) adc difference, (c) pca difference in principal direction, (d) normalized signal difference, (e) normalized adc difference and (f) PCA/FA metrics.

### Signal attenuation difference and normalized difference

The difference metric is a summation of the difference in signal attenuation over all gradient directions  $i$ . A normalized version of this metric divides the difference for each gradient direction by the sum of the two values. This results in a difference relative to the signal attenuation. Figure 3.12 (a) & (b) show the difference and normalized difference metrics respectively.

### ADC and normalized ADC

We developed the ADC based difference metrics to represent the difference in diffusion. This gives more insight in the change in diffusion instead of the signal attenuation as with the difference metric mentioned above. The normalized version divides the difference by the sum of the ADC values of both datasets. Again this is to relate the difference to the ADC. Figure 3.12 (c) & (d) show the ADC and normalized ADC difference metrics respectively.

### PCA

The above mentioned metrics only tell something about the signal attenuation or derived ADC. We developed a higher level difference metric which reflects

difference in the underlying diffusion process rather than the signal attenuation. This metric is based on the PCA (see section 2.3.3). For each voxel, a PCA analysis is done for both datasets. The dot product is calculated between the principal eigenvectors of both datasets. This results in a scalar measure for the deviation in the principal eigenvector direction.

The dot product is used in order to provide a metric for the difference. The dot product ranges from 1 to -1 considering a difference of 0 to 180 degrees. The eigenvectors are prone to flip because of the symmetric nature of glyphs. This effect is compensated for by using the absolute value of the dot product. There are however multiple cases which are not correctly interpreted by this measure. These include a flip in major eigenvector when the voxel is highly planar anisotropic or when the voxel is highly isotropic. The PCA/FA difference metric attempts to address this problem.

### PCA/FA

From thorough exploration of the data we observed four different classes which can be distinguished for differences between two glyphs. In an effort to quantify these different classes, we developed the PCA/FA difference metric.

*Theory* – Considering a voxel at the same position in two datasets, a difference in anisotropy is the most significant. For example, a transformation from linear anisotropy to spherical anisotropy would be classified this way. This indicates a serious change between the two datasets. When the change in anisotropy is low, the principal diffusion components can be used to identify differences. These can be differences in linear anisotropy, planar anisotropy or spherical anisotropy. For a difference in linear anisotropy, the deviation in principal component describes the difference for the voxel. For the planar case however, the first two eigenvalues are almost equal which limits detection of one main diffusion direction. For this case, the deviation in vectors normal to the plane can be used. The low anisotropy case is least significant because both voxels describe near isotropic diffusion.

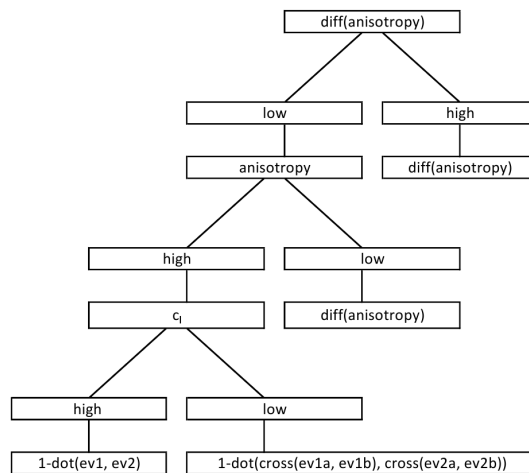


**Figure 3.13:** Difference classification decision tree for the PCA/FA difference metric.

*The metric* – We used the above mentioned theory to create a decision tree for the classification which is shown in figure 3.13. The four distinguished cases are, ordered to significance of the class:

1. Difference in anisotropy
2. Difference in linear anisotropy
3. Difference in planar anisotropy
4. Difference in spherical anisotropy

Using the FA as a measure for the anisotropy, the first case uses the difference of the FA of both voxels as a scalar difference value. The FA of the first voxel is used to distinguish between case 4 and cases 2 and 3 whereas the  $c_l$  value is used to distinguish between case 2 and 3. The second case then uses the dot product of the principal difference component of both voxels as scalar difference value. The third case limits the use of the principal diffusion component because the first two eigenvalues are almost equal. For this case, the vector normal to the plane is calculated first using the cross product. Then the dot product for the normal vectors of the two voxels is used as the scalar difference value for the metric. For the last case, the difference in FA is used as scalar difference value. The scalar range of the metric is show in figure 3.14.

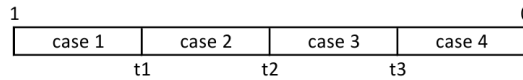


**Figure 3.14:** Scalar range for the PCA/FA difference metric.  $t_1$ ,  $t_2$  and  $t_3$  indicate the thresholds between the difference classes.

### 3.2.2 Global difference visualization

The difference metrics discussed in the previous section can be visualized in 2D or 3D. A 2D solution, using a slice viewer, is straightforward but limits the user's view to a single slice instead of the whole dataset. Examples in figure 3.12 show slices using different difference metrics.

Using 3D volume visualization or rendering of isosurfaces allows the user to rapidly localize areas of interest in the whole dataset.

Using a 3D field of scalar values, isosurfaces are often used to visualize a constant value in the 3D space (see figure 3.15(a)). Multiple isosurfaces can be used to visualize different aspects or intensity levels of the data. An example is shown in figure 3.15(b).

An alternative to isosurface rendering is volume visualization. This more advanced technique uses a opacity function and a color function (also known as transfer functions) to associate opacity and color with each voxel. The volume is then rendered using ray-casting. Areas with large differences appear as small cloud-like features in the 3D space. Because of careful definition of both opacity and color functions, these clouds are partially transparent showing the colors of inner values as well. This allows the user to rapidly identify a cloud of interest because of its size and color.

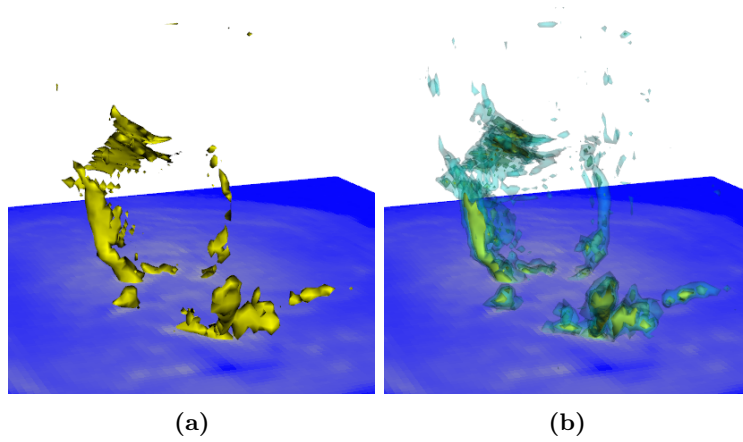


**Figure 3.15:** Isosurface visualization of difference metric showing (a) 1 isosurface and (b) 3 isosurfaces.

It is complex to specify suitable transfer functions, hence the definition of these functions can be time consuming. For this reason we implemented a simplified specification of the opacity transfer function technically based on two configurable parameters: the center and range. These parameters can be used interactively which offers flexibility and rapid identification of areas of interest.

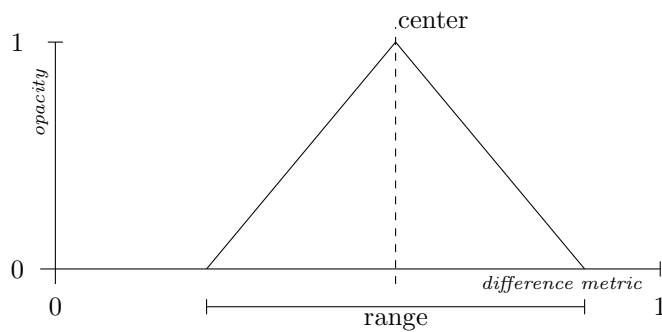


**Figure 3.16:** Illustration showing the range and center parameters for the opacity function for the volume visualization.

The center and range parameters are best explained using the illustration in figure 3.16. The opacity of each difference metric value is determined by this graph. The center determines the value which is completely opaque. Every point outside the center but inside the range is given a certain opacity determined by the distance from the center value. The color function is automatically adapted to fit the range of the opacity function. The color function used is adapted from the perceptually linear color scale as described in section 3.1.2.

Figure 3.17 shows how the parameters affect the volume visualization of the difference metric.

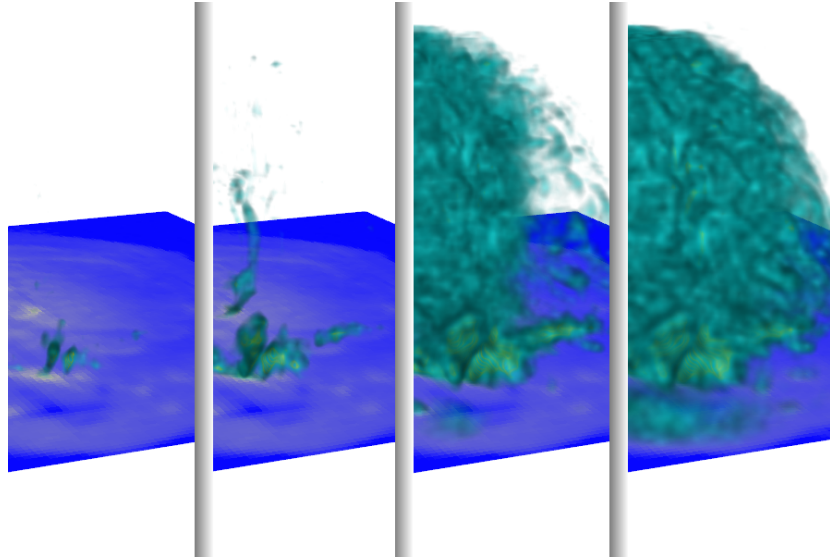


**Figure 3.17:** Interactive modification of center and range parameters of the transfer functions for the volume visualization. From left to right, the image shows decreasing threshold values increasingly revealing smaller differences.

### 3.2.3 Comparative glyphs

Besides new glyph representations for the direct visualization of HARDI data, we developed new glyph representations specifically for comparative visualization of HARDI data. These are the projected arrows representation and the colored and partial spheres representations. These glyphs are specialized in visualizing directionally dependent data of the difference between the datasets.

#### Projected arrows

The projected arrows representation is derived from the arrows representation (see section 3.1.1). The first dataset is presented with arrows for each of the gradient directions. Each arrow is scaled to the signal attenuation measured in that gradient direction and is colored gray. Spheres are then used to represent the difference between the two datasets which are projected on the arrows. The spheres are scaled to the difference between the datasets and colored to the sign of the difference, blue for negative and yellow for positive.

The result of this method is that the spheres representing the differences will group together forming features on a particular side of the glyph. This indicates a general increase or decrease on that side. For a single glyph, this representation is useful to see changes in a global direction. When used with multiple glyphs, trends can be explored in the data as multiple glyphs might expose the same directional difference data. Due to the complex nature of the representation, exploring a large number of glyphs is computationally expensive.

Figure 3.18 shows examples of a glyph with general increase (a) and decrease (b) in signal attenuation.

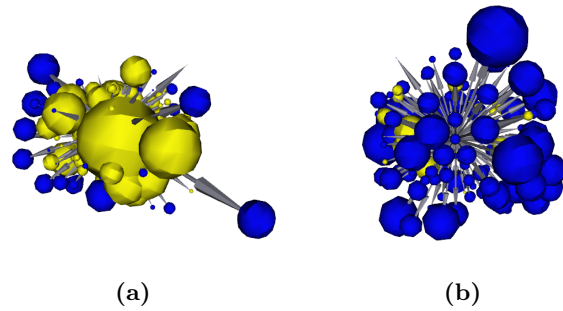


**Figure 3.18:** Projected arrows representation showing overall (a) increase and (b) decrease in signal attenuation.

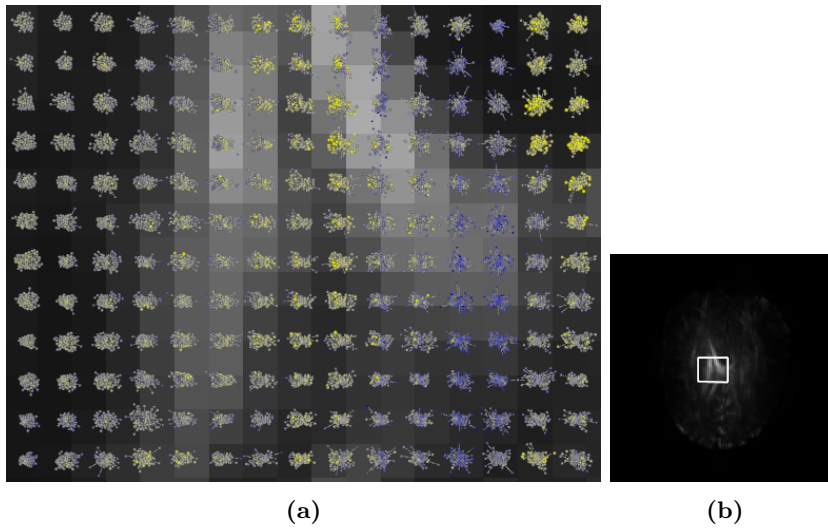


**Figure 3.19:** (a) shows global scale trends in signal attenuation change over multiple glyphs. The metric shown in (a) & (b) is the signal attenuation difference metric.

### Partial and colored spheres

The projected arrows representation results in performance loss when used on larger scale. Therefore we developed two additional comparative glyphs for exploring directional differences on a large scale. These are the partial spheres and colored spheres representations. The partial spheres representation consist of hexagonal shapes distributed according to the gradient directions. These are placed at unit distance from the origin to form a sphere. The color represents the difference between the first and second dataset.

Similarly to this, the colored spheres map the difference between the datasets to color on the sphere. The sphere however now consists of a single geometry where the number of vertices is equal to the number of gradient directions.

The vertices of the sphere do not coincide with the gradient directions. The `vtkKdTreePointLocator` class is utilized to lookup the closest gradient direction for a vertex based on the kd-tree algorithm. For each vertex, the closest gradient direction is determined. Then the corresponding color of that gradient direction

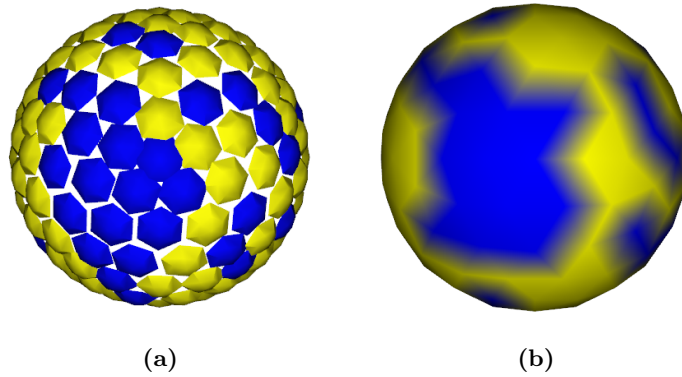


**Figure 3.20:** The partial (a) and colored (b) spheres glyph representations.

is mapped to the vertex.

The partial and colored spheres representations are shown in figure 3.20 (a) & (b) respectively.

### Shading

By default, Gouraud shading interpolation is used between the vertices of the colored spheres representation to color the complete sphere. This results in ambiguous colors on the sphere as colors blend between the vertices.

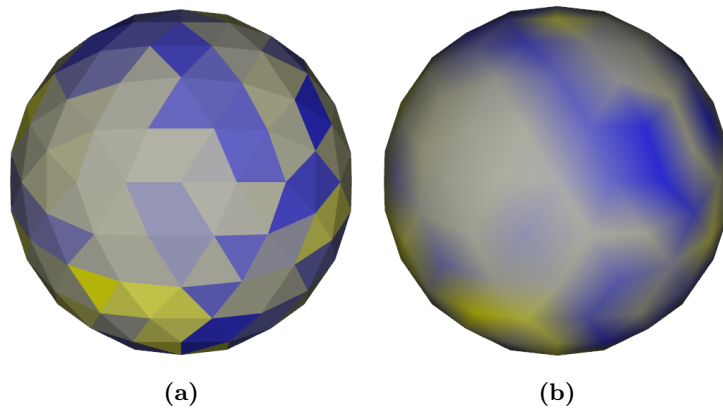


**Figure 3.21:** Comparison between flat and interpolated shading. (a) shows flat shading and (b) shows Gouraud shading interpolated

We added an option to enable flat shading which disables the color interpolation. This results in clear color values for the faces of the sphere. A comparison between flat shading and Gouraud shading is shown in figure 3.21.

### 3.3 Multiple linked views

Multiple views are an efficient way of providing the user with data presented with different representations at the same time [Mun09]. We developed a new layout with four views which can be used independently for data exploration using different glyph representations. The views can also be linked in terms of focal point, orientation and zoom level of the view. We also developed a 3D linked cursor which can be used for determining the location in the dataset and to explore gradient directions.

#### 3.3.1 Linked views

We developed a multiple views setup in a layout with four views. The layout of our implementation of the multiple linked views is shown in figure 3.1. One of the views is selected as the master view. Two options are available: link/unlink the views together and link/unlink the first view with respect to zoom level.

When the four views are linked, all other views are synchronized to the master view in terms of focal point, orientation and zoom level. For each view a different glyph representation can be selected providing flexibility to the user for data exploration.

When zooming in to single glyph level, context is lost and the location in the dataset might become unclear. Therefore we included an option to unlink the zoom synchronization with the top-left view. This way, the top-left view can be used as overview of the whole dataset providing context for the other views (see figure 3.1). The focal point and orientation still remain linked for spatial reference.

#### 3.3.2 Linked 3D cursor

We developed a 3D linked cursor to allow for spatial reference in the visualization. A location can be picked which is then displayed using a 3D crosshair. The crosshair is synchronized and shown in all views, scaled to fit the view's zoom level. An example is shown in figure 3.22.

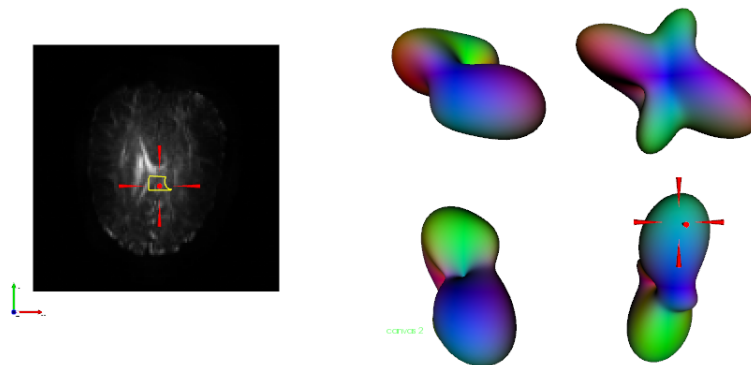


**Figure 3.22:** 3D cursor. The left view shows the difference metric with selected ROI (yellow). The right view shows q-ball glyphs with the 3D cursor relating the spatial position to the full slice in the left view.

We also designed the 3D cursor to allow for comparing gradient directions over multiple voxels. This technique is available for all our new glyph representations except for the arrows (PCA) glyph, the power crust surface glyph and the colored spheres glyph. Gradient direction selection is done by selecting a feature associated with a gradient direction of a glyph (i.e. arrow, sphere, etc.) with the 3D cursor. The selected gradient direction across all voxels in the ROI is then highlighted red for comparison. An example of this technique is shown in figure 3.23.

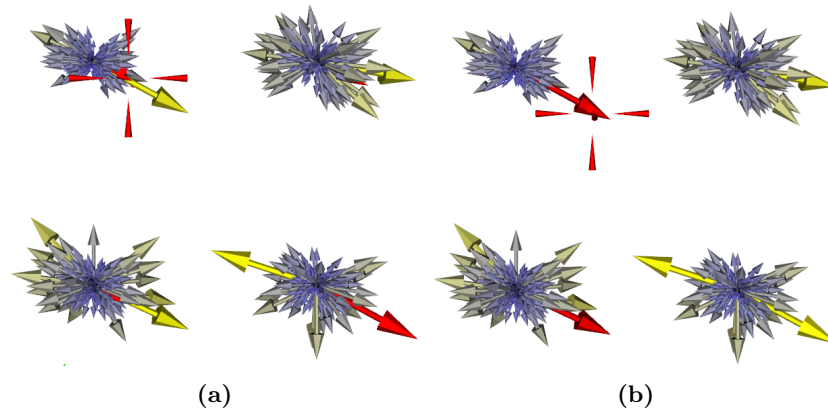


**Figure 3.23:** Gradient direction selection over multiple voxels.

The 2D and 3D slice view can also be set to display a particular gradient direction. When a gradient direction is selected, the selection is linked to the slice viewer when the gradient direction is shown. The user can then compare the signal attenuation in a particular gradient direction on the whole slice. Figure 3.24 shows this principle.

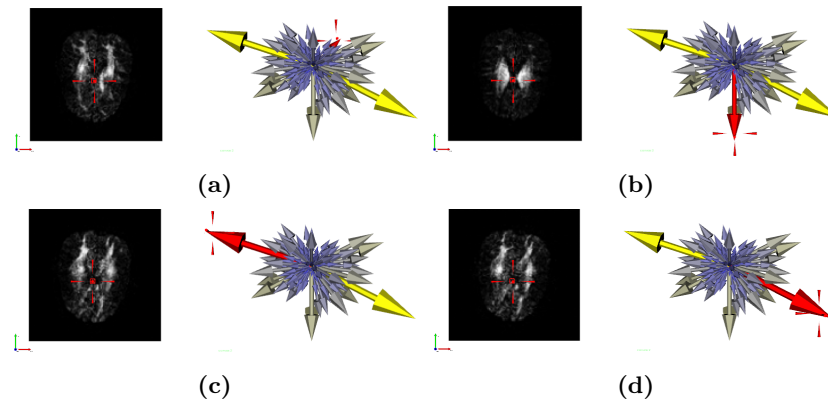


**Figure 3.24:** Gradient direction selection. (a) Shows the gradient slice view on the left and arrow representation of a single voxel on the right. (b), (c) & (d) Show various selected gradient directions.

# CHAPTER 4

---

## IMPLEMENTATION

For this project we used the DTITool software framework (A. Vilanova et al., Biomedical Engineering, TU/e). We extended DTITool with new techniques as described in chapter 3 to address the research goals for this project.

This chapter discusses the technical details of the implementation. The data conversion pipeline will be discussed which converts data from the scanner to DTITool native format. We developed the RFS Tools custom conversion package for the first stage of the conversion pipeline.

Details on the RFS Tools are explained. Then the implementation of our developed techniques in DTITool is discussed.

### 4.1 Data formats

There are several established medical data formats supporting DWI data modalities. These include the DICOM, NifTI-1, ANALYZE and PAR/REC formats.

The Digital Imaging and Communications in Medicine (DICOM) [Med] is the most extensively used data format for medical imaging data. Its origin dates back to the 1970s. A new standard was required for the increasing use of digital images for a broad range of different devices and manufacturers. DICOM can be used to archive image data as well as other information objects like patient information, reports or waveforms and defines protocols for network communications.

The Neuroimaging Informatics Technology Initiative (NifTI) created another data format called NifTI-1 which is specialized to archive medical image data [Neu]. The format is a spin-off from the ANALYZE format developed at Mayo Clinic [May]. NifTI-1 was primarily designed to support functional Magnetic Resonance Imaging (fMRI) data while still being compatible with the well known ANALYZE 7.5 data format. The NifTI-1 format is versatile and can be used for a wide range of medical image data besides fMRI. The files associated with the ANALYZE format are a .hdr and .img file for header and imaging data respectively. The NifTI-1 format has the same formats while a single .nii file can also be used which contains both the header and the image data in one file.

The PAR/REC format is developed by Philips and is used as medical image data for the 7 Tesla MRI scanner. The format is divided into a .par file which acts as a header file. The corresponding .rec file contains the actual image data.

The DTITool native format consists of a tensor dataset format and a HARDI dataset format. The tensor dataset consists of a .dti header file and .dat data files. The HARDI dataset consists of a .hardi header file and *gxx.dat* image files where *xx* is the gradient number.

## 4.2 Data conversion pipeline

The output of the scanner at the LUMC generates data in the PAR/REC format. This has to be converted to DTITool native format. The BioMedical Image Analysis (BMIA) group of A. Vilanova et al. from the TU/e provided a conversion tool which can convert NIfTI-1 format into DTITool native format. We have extended this pipeline to convert data from the PAR/REC to NIfTI-1 format which completes the conversion pipeline.

The complete pipeline is given below in figure 4.1. For the light-blue lines,

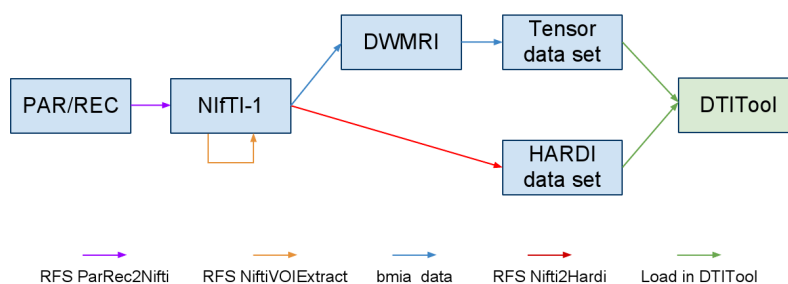


**Figure 4.1:** Schematic of the conversion pipeline from PAR/REC to native DTITool format.

the conversion package provided by the BMIA group is used. These have the DWMRI data format, a custom format, as intermediate step after which a tensor set is created. As a last step, the Tensor and HARDI data sets are loaded into DTITool. The remaining steps use the RFS Tools package which is explained in the next section.

## 4.3 RFS Tools

We developed the RFS Tools custom conversion package to complement the conversion pipeline. The RFS Tools package consists of four different programs, three for data conversion and one as a convenience utility for reading NIfTI-1 header information. The RFS Tools are developed using Visual Studio 2008 and are written in the *c#* programming language. The RFS Tools include:

- RFS ParRec2Nifti
- RFS NiftiVOIExtract

- RFS Nifti2Hardi
- RFS NiftiHeaderReader

The *RFS ParRec2Nifti* tool allows for conversion from PAR/REC to NIFTI-1 file format. Figure 4.2 shows the application window.

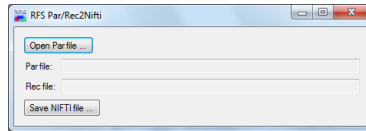


**Figure 4.2:** RFS ParRec2Nifti.

RFS ParRec2Nifti also produces a .bvec file which contains the gradient directions. The PAR/REC file however does not contain the correct gradient directions when using a custom gradient distribution. Instead of using the created .bvec file, a correct .bvec can be created from the gradient directions provided to the scanner for the acquisition.

While a full DWI dataset can be quite large, loading time often became a problem during development. Therefore we developed the *RFS NiftiVOIExtract* tool. RFS NiftiVOIExtract reads the data space which is user configurable in our tool (see example in figure 4.3). A subset of the data is then extracted and written to a new NIFTI-1 file. The ability to load a smaller subset from the original dataset speeds up the overall development process.

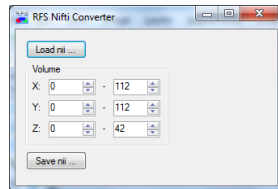


**Figure 4.3:** RFS NiftiVOIExtract.

The *RFS Nifti2Hardi* conversion tool is used to convert NIFTI-1 files to a HARDI dataset which can be loaded into DTITool. Empirical testing showed that HARDI data from NIFTI1 files had to be flipped in the  $y$  and  $z$  directions to line up with the corresponding tensor dataset. Therefore an option was included to flip the  $x$ ,  $y$  and/or  $z$  axes. Also options are available to read statistics or divide all values by a particular number.

The statistics option creates a list with the range of each gradient direction (including  $B_0$ ). The values can also be divided by a user defined number when converting. A  $b$ -value should be manually entered by the user because it is not part of the NIFTI-1 specification. The  $b$ -value is added to the native DTITool format. The application window is shown in figure 4.4.

We developed *RFS NiftiHeaderReader* for reading NIFTI-1 file header information. The tool supports both single NIFTI-1 .nii files and .hdr/.img combination files. Also drag&drop functionality is included for improved usability.

## Chapter 4. Implementation

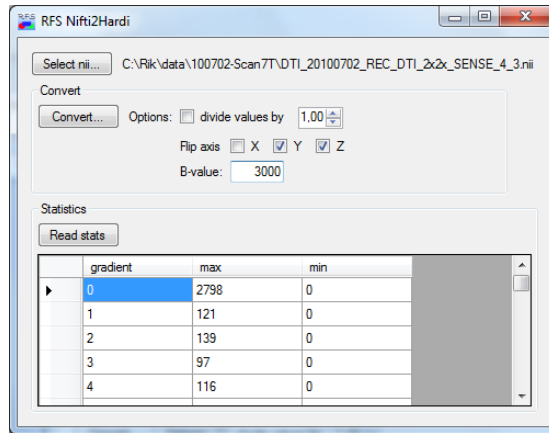


Figure 4.4: RFS Nifti2Hardi.

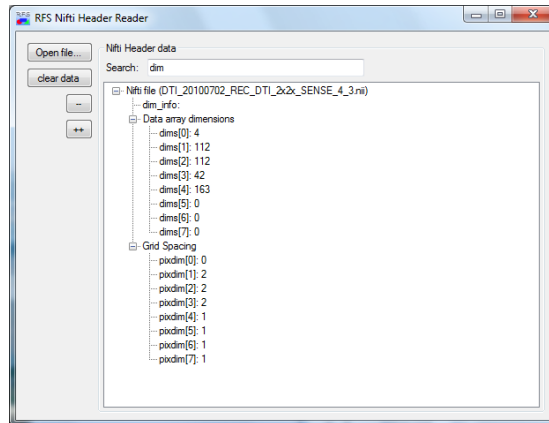


Figure 4.5: RFS NiftiHeaderReader.

The header(s) are read in the program and displayed to the user as a tree, grouping several properties like dimensions and spacing. A search option allows on-the-fly searching for header entries filtering out irrelevant entries (see the example in figure 4.5). This allows the user to quickly find file properties of interest.

### 4.4 DTITool

The DTITool framework provides support for medical image processing and visualization techniques such as DTI and HARDI data, using state-of-the-art algorithms [PPvA<sup>+</sup>09]. Techniques like glyph visualization for both tensor and HARDI data are supported as well as fiber tracking and isosurface rendering.

First the runtime system of DTITool is discussed with all required software packages. Then several issues are explained which came up while extending

DTITool.

#### 4.4.1 Run-time system

DTITool requires several software libraries to be installed before creating a custom build. The libraries are listed in table 4.1.

Name	Description	Version	Website
VTK	The Visualization Toolkit	5.4.2	<a href="http://www.vtk.org/">http://www.vtk.org/</a>
QT	Application and UI framework	4.6.2	<a href="http://qt.nokia.com/">http://qt.nokia.com/</a>
gsl	GNU Scientific Library	1.13	<a href="http://www.gnu.org/software/gsl/">http://www.gnu.org/software/gsl/</a>
GLEW	The OpenGL Extension Wrangler Library	1.5.4	<a href="http://glew.sourceforge.net/">http://glew.sourceforge.net/</a>
log4cplus	log4j c++ port	1.0.4 rc7	<a href="http://log4cplus.sourceforge.net/">http://log4cplus.sourceforge.net/</a>
zlib	Compression library	1.2.4	<a href="http://www.zlib.net/">http://www.zlib.net/</a>
CMake	Build system	2.8	<a href="http://www.cmake.org/">http://www.cmake.org/</a>

**Table 4.1:** Software libraries used for DTITool development.

Due to memory limitations of the Windows XP 32-bit machine, software was built and used on a Windows 7 64-bit machine.

#### 4.4.2 GUI layout

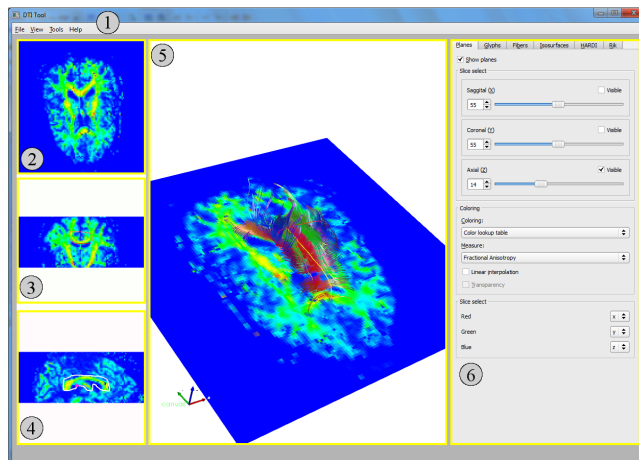


**Figure 4.6:** DTITool main window.

The GUI layout of DTITool is shown in figure 4.6. Area (1) shows the menu bar with pull-down menus. Area (2), (3) and (4) contain three 2D slice views. These are the axial (2), coronal (3) and sagittal (4) slice view. Area (5) contains the 3D view. On the right side is area (6) which features several tabs with controls to alter the visualization parameters.

Area (2), (3), (4) and (5) are user configurable and can be changed to several layouts. These include:

- All, large 3D
- All, same size

## Chapter 4. Implementation

- 3D
- Sagittal (X)
- Coronal (Y)
- Axial (Z)
- Multiview (4 3D)

The first option is set by default which is shown in figure 4.6. The last option is the multiple coupled views layout which is shown in figure 3.1.

### 4.4.3 User interaction

User interaction in DTITool can be done using GUI components, with the mouse in the 2D/3D views or by means of the keyboard. The user can alter the visualization using parameters on one of the tabs in the GUI. The parameters are grouped together on tabs to have a convenient overview of relevant parameters for specific visualizations.

Interaction for the 2D and 3D views is done using the mouse. The user can translate, rotate and zoom using the mouse. For the multiple views layout, a particular view can be selected as the master view. This can be done by just clicking on the view, selecting it using the Rik tab (see section 4.4.4) or using one of the key bindings.

A range of key bindings is available to activate/change certain options. Two tables describe all the mouse (table B.1) and keyboard (table B.2) actions possible with DTITool. These are included in appendix B.

### 4.4.4 Rik tab

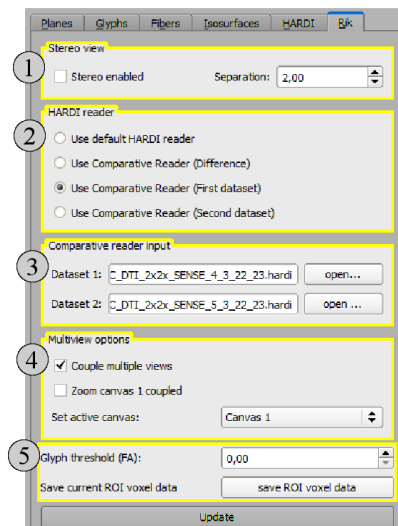


Figure 4.7: The Rik tab.

We grouped most of the new options for the GUI on a new tab, the Rik tab. The layout of the tab is shown in figure 4.7. All areas will be briefly explained.

At the top, area (1) contains a stereo vision option. This allows DTITool to display anaglyph (red/cyan colored) images where the user is able to specify the separation between the eyes. This feature is included to increase the 3D perception of the visualization.

Area (2) sets the HARDI reader to be used. These include the default HARDI reader or the comparative reader. The default reader allows to load a single HARDI dataset. Most visualization techniques, including the direct HARDI visualization techniques, can be used with a single HARDI dataset.

Using the comparative reader enables the use of comparative visualization techniques. The user can select the first or second dataset which is then used for visualizations for a single dataset. The difference can be used to use the difference of the datasets with HARDI visualization techniques for a single dataset.

Area (3) allows the user to load 2 datasets for comparative visualization. When files are selected, the option *comparative reader (first dataset)* is automatically selected to be used for visualizing the data. The data is loaded after clicking on the *update* button.

Area (4) allows the user to select a view as master view, couple or de-couple the multiple views and couple or de-couple the zoom of the top-left view. A more detailed description of these options is discussed in section 3.3.

In area (5), a threshold on the FA can be set and allows for ROI export. The FA threshold value is used for glyph visualization and will exclude voxels with a low FA value from the visualization. A ROI can be exported to a set of files. These files can then be used in other applications for further analysis and exploration of the data. This function will be covered in more detail in section 4.5.6.

## 4.5 DTITool implementation details

### 4.5.1 Glyph shapes

Glyph shapes are created using polygon models. The `vtkGlyph3D` class is utilized which copies a source object to each of the defined points in its input. When using points as defined by the gradient direction and scaled to their respective signal attenuation, the resulting representation is a direct visualization method for the signal attenuation. Different source objects like the `vtkSphereSource` or `vtkCubeSource` are used for the models.

#### Glyph coloring problem

To use colors for the direct glyph representations, an array with scalar values is used for color specification. A lookup table is then utilized to select the correct color and opacity (see section 3.1.2) based on the scalar values. When the array is an unsigned character array however, the lookup table is omitted and the values are used as RGB values directly. This principle gave unexpected results with early implementations of the glyph representations.

In our final implementation we assign a single dimension array to the glyph with indices (range  $[0, 255]$ ) to the lookup table. The application is explicitly set to map colors using the lookup table.

### Coloring scale

A perceptually linear color scale is used for our glyphs as described in section 3.1.2. For the implementation, the RGB values of the color scale were obtained from the color center [Lev]. This color scale is used with the new direct and comparative glyph representations.

### 4.5.2 Multiple coupled views

One of the main concerns for the multiple coupled views was the synchronization of the views and the 3D cursor. We implemented a custom interactor style, the `vtkLinkedViewsInteractorStyle` class. This class contains two methods, `syncCameras` and `sync3DCursors`, to support synchronization of the views and the 3D cursor.

The multiple views all have a VTK pipeline which is shown in figure 4.8. The `HARDIGlyphRepresentation` class contains the visualization parameters. When a view is selected, the GUI is updated to reflect the parameters of the visualization stored in the corresponding instance of the `HARDIGlyphRepresentation` class.

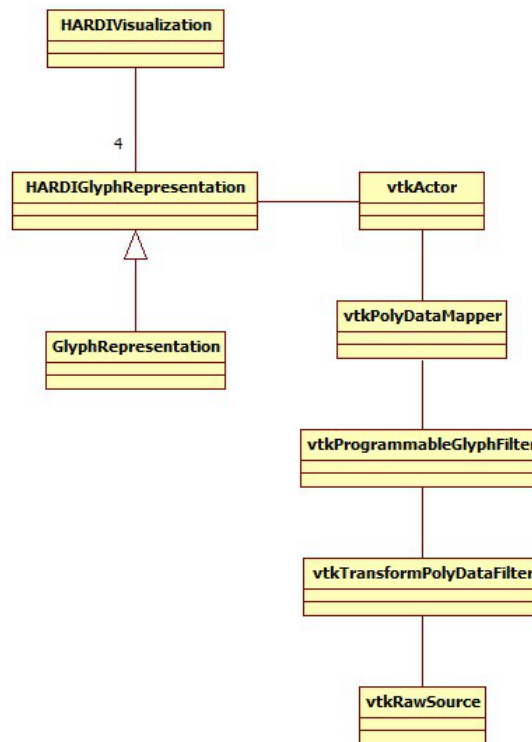


**Figure 4.8:** A schematic diagram of the multiple linked views VTK rendering pipeline. The `HARDIVisualization` class features four instances of the `HARDIGlyphRepresentation` class to have four independent rendering pipelines.

To update the GUI with the correct visualization parameters, direct method invocation is used when a view is selected using the Rik tab (see section 4.4.4).

When selection of a view is done by clicking on one of the views, an observer pattern is used. The Rik tab is added as an observer to the view to receive the view selection event. This allows the GUI to be updated to display the selected view and the corresponding glyph representation parameters.

### 4.5.3 Slice viewer and gradient directions

We extended the 2D and 3D slice views to display gradient direction slices. DTITool contains two 3D slice viewers, one for tensor (Planes tab) and one for HARDI (HARDI tab, planes tab). When the HARDI planes are set visible, the slice selection can be synchronized to the 2D slice viewer. This enables the correct slice to be visible on the 2D slice viewer for quick ROI drawing.

When exploring comparative HARDI data with the multiple views layout, the HARDI slice view can be used to display the first or the second dataset. Key bindings ('1' and '2' keys) allow for rapid switching between the two datasets.

### 4.5.4 Comparative visualization

We first developed a data reader which featured the difference of two input datasets as its output. This difference could be visualized with subsequent visualization methods in DTITool. The method however limited visualization options because the input datasets were only available to the reader.

We developed the `vtkHARDIComparativeReader` class as a solution to this problem. This reader used two class variables of type `vtkHARDIReader` for two datasets. The output of the comparative reader is the difference of both datasets. Methods were introduced to access the two `vtkHARDIReader` classes so the data of the two datasets could be used separately as well. This allowed for more flexibility when implementing the difference metrics and comparative glyphs.

### 4.5.5 PCA/FA difference metric

Our implementation of the conceptual PCA/FA difference metric described in section 3.2.1 is shown in table 4.2. This table will be explained in more detail.

Range	Condition	Output
0	$0.1 -  FA_1 - FA_2  < 0.05$	$ FA_1 - FA_2 $
0.1	$0.3 - FA_1 < 0.3$	$FA_1$
0.3	$0.7 -  c_{l1} - c_{l2}  < 0.1$	$1 - \text{dot}(ev_{1a}, ev_{2a})$
0.7	1.0 - other	$1 - \text{dot}(\text{cross}(ev_{1a}, ev_{1b}), \text{cross}(ev_{2a}, ev_{2b}))$

**Table 4.2:** Range specification of our implementation of the PCA/FA difference metric. The variables used are: FA=Fractional Anisotropy,  $c_{li}=c_l$  of  $i^{\text{th}}$  dataset,  $ev_{ij}=j^{\text{th}}$  largest eigenvector of  $i^{\text{th}}$  dataset.

If there is a small change in anisotropy, the first case is used to compute the difference. For the second case, there voxel is highly isotropic. The FA value itself is then used as the difference. The third case is used for linear anisotropic voxels where the change in angle is small. Then the deviation of the angle is computed as the difference. For the fourth case, the voxel is planar

anisotropic. The difference is then computed as the deviation of the planes from both datasets.

Testing of the PCA/FA difference metric reveals that determining the thresholds proves to be difficult. Also the range for a particular class in the difference metric is difficult to determine. Our implementation is a first attempt to determine values for the thresholds and the ranges to reflect relevant differences.

### 4.5.6 ROI export function

We developed an export function which exports the signal attenuation values of the current ROI to a file. Data values of both datasets are written if a two HARDI datasets are loaded. Table 4.3 gives descriptions of the files created.

file	description
<i>First dataset A</i>	
<filename>_datasetA_gradients.dat	File with gradient direction vectors.
<filename>_datasetA_signal.dat	File with the raw signal attenuations of each voxel.
<filename>_datasetA_voxelpos.dat	File with a grid defining the voxel locations.
<i>Second dataset B</i>	
<filename>_datasetB_gradients.dat	File with gradient direction vectors.
<filename>_datasetB_signal.dat	File with the raw signal attenuations of each voxel.
<filename>_datasetB_voxelpos.dat	File with a grid defining the voxel locations.

**Table 4.3:** Files generated with the ROI export function. <filename> denotes the filename provided by the user.

The export function exports the signal attenuation values, the gradient directions and the voxel locations. The file format is chosen in a way that the files can be loaded in Matlab [Mat]. More information about the files and the exact file format can be found in appendix C.

# CHAPTER 5

---

## RESULTS

We performed a case study as part of the evaluation of the implemented techniques in DTITool. First a brief description will be given of the acquired MRI scan used for evaluation of DTITool. Then the results of the case study will be presented. Improvements based on the case study are discussed next. We have performed in-depth exploration of the data for further evaluation of the tool. Our observations will conclude this chapter.

### 5.1 Acquisition

Early in the project we had scans available with 60, 128 and 162 gradient directions provided by the department of radiology of the Leiden University Medical Center (LUMC). We used them to start testing the new representations and for early testing of the comparative visualization techniques. For comparative visualization, two adjacent slices of the dataset were extracted. Later on we acquired new scans for evaluation of the implemented techniques.

#### 5.1.1 Scan setup

The scanner used for the experiments is a Philips Achieva 7 Tesla whole body MRI scanner. The scanner, situated at the C.J. Gorter center of the LUMC, was used to make two back-to-back scans of the brain. Between the scans, the subject remained in the same position and for both scans exactly the same parameters were used. Image registration was not included for this acquisition.

#### 5.1.2 Scan parameters

Determining the scan parameters was not straightforward due to the experimental status of the 7 Tesla MRI scanner. More specific, the questions were how many gradient directions and the  $b$ -value to use with the acquisition.

We asked Vesna Prčkovska from the department of Biomedical Engineering of the TU/e for advice on these parameters because of her experience with these acquisitions [PRP<sup>+</sup>08]. A number of 50-90 gradient directions would be

sufficient for the acquisition. With a 162 gradient direction scheme already available, we decided to use 162 directions. The  $b$ -value should not be too high as to guarantee a good signal-to-noise ratio (SNR). Based on Vesna's advice, we selected  $b = 3000$  for our acquisition.

The acquisition was done using 162 gradient directions with a  $b$ -value of  $b = 3000$  and one  $B_0$  weighted image. The 162 directions were distributed according to the folded icosahedron gradient encoding scheme.

The dimensions for the acquisition are  $112 \times 112 \times 42$  (sagittal, coronal and axial) with a spatial resolution of  $2.0mm \times 2.0mm \times 2.0mm$ . We acquired two scans where the time in between was kept as small as possible (order of one minute). The scan subject tried to move as little as possible during this break.

## 5.2 Case study

### 5.2.1 Introduction

The case study is intended to provide an evaluation of the effectiveness of DTI-Tool in answering the main research question. Within the following sections, DTI-Tool will be referred to as the tool. Furthermore, with new representations is meant the collection of the direct and comparative glyph representations implemented in DTI-Tool. These include: arrows, arrows (original), arrows (PCA), cone, arrows (projected), spikes, gradient cube, spheres, dots, power crust surface and power crust surface + dots.

This case study is based on the principles and terminology for case study research as described by Yin [Yin08]. The next two sections contain propositions used for the case study as presented to the participants and the results of the case study.

### 5.2.2 Case study definition

#### Main research question

*"How can direct and comparative visualization techniques contribute to the understanding of noise artifacts in HARDI data"?*

#### Case

"Use of DTI-Tool by an expert MRI physicist."

#### Propositions

- The volume visualization allows for intuitive exploration and quick identification of areas with large differences.
- The difference metrics used for the slice view and volume rendering allow for rapid detection of areas with large differences.
- Using the ROI drawing in the 2D views in combination with the (3D difference metric) slice view and/or volume rendering allows for fast zooming into areas of interest.
- Per-voxel data exploration is more effective using multiple (coupled) views instead of using a single view.

- The new representations present per-voxel data in a visual more effective way than representations used for reconstructed HARDI data using ADC, QBall, DOT non Param or DOT.

New representations:

- Arrows (normal, original, PCA, projected)
  - Cone
  - Spikes
  - Gradient cube
  - Spheres
  - Spheres colored
  - Power crust surface + dots
  - Power crust surface
  - Dots
- The color scales used for the new representations clearly present the meaning of the data and can be easily adapted to the users needs.
  - Using the linked cursor and the ability to couple/uncouple the multiple views, context is preserved while exploring a specific gradient direction of the data.
  - By providing the user with comparative and direct visualization techniques on HARDI data, the tool can effectively be used in studies for better understanding noise artifacts in HARDI data.

### 5.2.3 Results

We performed the case study on Friday July 16th at the LUMC. Present at the case study were:

Thijs van Osch (TvO) (Associate professor, C.J. Gorter center, LUMC)

Itamar Ronen (IR) (Associate professor, C.J. Gorter center, LUMC)

Julien Milles (JM) (Assistant professor, Dept. of Radiology, LUMC)

Charl Botha (CB) (Assistant professor, EEMCS Computer Graphics, TU Delft)

An interactive discussion was setup where TvO, IR and JM commented on principles from the propositions being shown with a live demo of DTITool. Each of the propositions will now be discussed with the proposition preceding in italic font.

---

*The volume visualization allows for intuitive exploration and quick identification of areas with large differences.*

---

*The difference metrics used for the slice view and volume rendering allow for rapid detection of areas with large differences.*

The first two propositions were commented on together by the participants. A first look at the slice view revealed that context should be included like a  $B_0$  for example. It should also be possible to change the metric. This is already possible but only tensor based metrics are included at the moment (i.e. FA). Another comment suggested that the ideal difference metric should be insensitive to anisotropy. IR explained that areas of difference can be located and often coincide with expectations. The ventricles for example can be located with noise because of cerebrospinal fluid (CSF). TvO commented that he is quickly getting a feeling for the data while using the slice view and volume visualization.

---

*Using the ROI drawing in the 2D views in combination with the (3D difference metric) slice view and/or volume rendering allows for fast zooming into areas of interest.*

The 2D slice view is not linked to the 3D slice view or the volume rendering. While the difference metric is only available at the 3D slice view and drawing of the ROI is only available at the 2D slice view, ROI drawing proves to be difficult. Possible solutions to this problem are making the difference metrics available for the 2D slice viewer and making it possible to draw a ROI on the 3D slice view.

There was also a comment on the arrow length of the arrows representation. The arrows are now scaled to the measured signal divided by the  $B_0$  measured signal. The scale factor should however become the Diffusion coefficient where the log is incorporated in the calculation.

---

*Per-voxel data exploration is more effective using multiple (coupled) views instead of using a single view.*

The coupled views were found to be an important tool. One of the suggested improvements is on data complexity when zooming out. When the area includes too many glyphs, lower resolution features should be used to represent the voxels.

The context view now available could be improved on but it is agreed that the function adds value to the visualization. It would also be convenient to be able to switch between datasets.

---

*The new representations present per-voxel data in a visual more effective way than representations used for reconstructed HARDI data using ADC, QBall, DOT non Param or DOT.*

TvO commented that this proposition is comparing apples and pears with respect to the representations. This was clarified by CB whereas this proposition is meant for the diffusion. TvO though liked the low level representations where he was shocked how different the data actually is. There seems to be a problem with the arrows (PCA) representation where the arrows did not start at the origin. The cubes representation was not considered to be a contribution whereas the spheres representation was found to share much redundant

information in the color, size and position of the object.

The power crust surface was found not to be correct because of holes and/or floating points. Also there was not a unique solution for the surface to be fitted on the diffusion measurements. The dots representation was found to be unclear where the user has to rotate the glyph to see the origin of the dots.

Coloring with significance thresholding was considered not to be a valuable addition. While the threshold is arbitrary, a suggestion was to make small values transparent so they could serve as context. With difference visualization however, the participants could imagine the significance thresholding useful to display the highest increases or decreases of the data.

---

*The color scales used for the new representations clearly present the meaning of the data and can be easily adapted to the users needs.*

The participants agree on this proposition that the differences were clearly presented by the color scales.

---

*Using the linked cursor and the ability to couple/uncouple the multiple views, context is preserved while exploring a specific gradient direction of the data.*

The selection of a single direction of diffusion using the 3D cursor which is then showed on the 3D slice view was thought of as a valuable addition. Though useful for exploration, a suggestion was made to show the gradient direction of both datasets instead of only one dataset as currently implemented. This would be useful to study artifacts.

---

*By providing the user with comparative and direct visualization techniques on HARDI data, the tool can effectively be used in studies for better understanding noise artifacts in HARDI data.*

The tool was thought to be a potential valuable addition to the main problems with HARDI data if registration is included.

---

Besides a discussion on the propositions, there was also some discussion on possible publications using the tool. One of the main topics was image registration which came up during the last proposition as well. Image registration is necessary for evaluation of the data using the tool.

Next to registration was that the diffusion coefficient needs to be used for the glyph values whereas the log function was not included in the calculations. For acquisition, there were also suggestions for full q-space or diminished q-space acquisition instead of q-ball as done for this evaluation.

## 5.2.4 Case study conclusions

The visualization of the difference metric using the slice viewer or the volume visualization was an effective tool for location of areas of interest. The visualization allowed the user to quickly get affinity with the data though it was suggested the 3D camera handling can be improved.

For ROI selection to be more effective, the 2D and 3D slice viewer needs to be linked. The 2D slice viewer additionally needs to be extended to display the difference metrics. ROI selection using the 3D slice viewer should also be considered a valuable addition. For values representing the diffusion process, the ADC should be used to calculate the diffusion coefficient.

Gradient direction exploration using the slice viewer combined with the selection method with the 3D cursor was considered a valued addition. The effectiveness can be increased however by allowing exploration of gradient directions of both datasets at the same time.

While the volume visualization was effective, there were insufficient options to link this to other context. This could be anatomical context as well as difference metric slice views for ROI selection or the  $B_0$  image. Expected features from the data could be extracted, such as the noise near the ventricles caused by CSF. This indicated an accurate visualization with respect to known data characteristics.

The multiple coupled views layout was found to be an important tool for data exploration. The function of the overview was agreed upon but also selected for improvement. The projected arrows representation was found to be effective for difference exploration but is computationally expensive for large ROIs. Low(er) resolution glyphs were suggested for improved performance.

The visual complexity of the visualization can be decreased with some minor modifications to existing representations or with new representations. In general, ambiguity and occlusion remain important issues for the glyph representations. Coloring was found to be representing data values effectively though including transparency as to discard insignificant data values could be beneficial. This also holds for significance thresholding which was only considered a useful addition for difference exploration.

The use of an export function could be beneficial to exploration of data using different software tools. The export function could for example export the ROI for further analysis in Matlab [Mat].

One of the main limitations was found to be the absence of image registration. Registration for HARDI data is difficult because the data is directional dependent. Several techniques have been proposed to solve this problem [APBG01, CVCM09].

### 5.2.5 Improvements based on case study

During the case study, several extensions and improvements were suggested. Most of these were improved or added in DTITool after the case study. This increased both effectiveness and efficiency of the developed visualization techniques. Each extension or improvement will be shortly discussed below.

#### Lower FA threshold

We added a threshold on the FA to exclude voxels with a low FA index. This option is added to the Rik tab which can be used in combination with the new glyph representations.

**Improved ROI selection**

One of the main issues was selecting a ROI based on the difference metric. The difference metrics could only be shown on the 3D slice viewer. We added the difference metrics to the 2D slice viewer as well. Areas of interest found in the 3D slice viewer or volume visualization can now quickly be linked to the correct location in the 2D slice viewer for ROI selection.

We also added the option to link the 3D HARDI slice viewer to the 2D slice viewer. This enables synchronization of the slice selection from the 3D HARDI slice viewer to the 2D slice viewer while exploring data using the 3D slice viewer.

**ROI export function**

For some specific questions about the data, further exploration of the HARDI data with an external tool is necessary. We developed an export function which exports the gradient directions, signal attenuation values and the spatial locations of the voxels. The files are suitable for use in Matlab [Mat], but can also be used by other tools. See appendix C for details on the file format.

**Use of ADC**

During the case study, an option 'invert signal' was available which inverted the measured signal attenuation. The option is replaced with the option to use the ADC instead of the signal attenuation. This enables the exploration of ADC values which reflect the underlying diffusion process.

**Improved comparative glyph representations**

We improved the comparative glyph representations in terms of performance and visual effectiveness. Based on the case study, we developed the partial spheres and colored spheres representations. These are discussed in section 3.2.3. We revised the projected arrows representation to improve on accuracy when using the new ADC option. The projected arrows representation is also discussed in section 3.2.3.

**Improved gradient direction exploration**

We improved the exploration of gradient directions by creating an option to rapidly switch between the datasets. This is implemented with the key combinations '1' and '2' when the gradient direction slice is displayed on the slice viewer.

We also improved on the gradient direction selection as all glyph representations (except the arrows PCA, power crust surface and colored spheres representations) support gradient direction selection. This allows the user to select a gradient direction when exploring the data using comparative glyph representations.

**Shading and transparency**

Transparency is added to the color scale to emphasize significant values of the data. These color scales can be used with both direct and comparative glyphs. These color scales are discussed in more detail in section 3.1.2.

We also added an option to disable shading interpolation for the glyphs. This option offers clear color values instead of the interpolated values. This technique is described in section 3.2.3.

## 5.3 Data analysis

This section first describes some common artifacts found in MRI images. Then observations will be discussed which are based on exploration of the HARDI dataset as discussed in 5.1.

### 5.3.1 Common data artifacts

Several common artifacts can be found in MRI data [Hor96, WKM08]. Each will be briefly described.

- **Chemical shift** – Incorrect registration of tissue, mostly caused by large difference in chemical properties such as water and fat. The borders between the two types of tissue appear dark or bright on the final image.
- **Motion artifacts** – Motion artifacts occur when the subject is moving during the acquisition. The final image is partly or completely blurred according to the area that moved. Ghost images may also appear in the phase encoding direction.
- **Flow artifacts** – Flow artifacts occur in areas containing fluid flows, for example blood or CSF. The fluid is experiencing the wrong phase changes because it flows out of the slice during the acquisition or to another place on the slice. The final reception of signal therefore has the wrong phase and results in a darker or brighter part of the image.
- **RF Noise** – Due to RF noise, the reception of signal phase is imperfect. This is caused by RF signal being captured from other sources, such as a not fully closed scanner room door. The signal phase changes are transformed by the Fourier transform and translate in for example diagonal interchanging darker and brighter lines in the final image.
- **$B_0$  inhomogeneity** – The  $B_0$  magnetic field is assumed to be homogeneous. Due to deviations in this field, spins are changed due to the Larmor relation. This results in signal changes in the final image. Common effects seen in images are deviations in the signal intensity and bending of features.
- **Gradient inhomogeneity** – Just as  $B_0$  inhomogeneity, the gradients can be inhomogeneous too. Damaged gradient coils or abnormal currents passing through the gradient may cause artifacts in the final image like a squeezed image.
- **Magnetic susceptibility** – Change in magnetic field due to magnetic susceptible objects, often metal such as titanium or stainless steel. The final image is distorted around these objects.

- **RF Inhomogeneity** – Variations in the RF signal intensity or the RF receiver coils result in undesired variations in the final image. When metal objects are present, these can restrict the RF signal reaching certain tissue which may result in signal voids in the image. These generally appear local and do not distort the complete image.
- **Partial volume effect** – Voxels containing multiple tissue types result in the weighted average of these tissue types. This effect is stronger with larger voxel sizes. Features tend to appear more blurred with partial volume effects. Decreasing the voxel size decreases the partial volume effect though the SNR becomes lower and scanning time increases for the same area of interest.
- **Phase wrapping/wrap around** – Part of the subject scanned which is outside of the Field Of View (FOV) is shown at the other side of the image, opposite the spatial location of the area. This effect is due to a FOV which is smaller than the area scanned. Some tissue outside the FOV is detected with the RF coil and wrapped around to the other side of the final image.
- **Truncation artifacts/Gibbs ringing** – Artifacts showing increased signal intensity at high contrast edges of tissue. These appear with small acquisition matrices where the echo is not fully decayed at the end of the acquisition window.
- **Magic angle** – Mostly seen in solids such as tendons and ligaments where fibers are at an angle of 55 degrees with the main magnetic field. The effect is mostly noticeable when using a short  $T_2$  time where the solid appears brighter.

### 5.3.2 Observations in the data

#### Motion between acquisitions

Figure 5.1 shows a motion artifact near the Corpus Callosum. Figure 5.1 (a) & (b) show colored spheres for the ADC difference derived from the signal attenuation. Figure 5.1 (b) also shows reconstructed fiber tracts of the Corpus Callosum as context.

From figure 5.1 (a), a line with glyphs following the Corpus Callosum can be observed which is mostly colored yellow. This indicates a increase in ADC in the second dataset.

Exploration of gradient directions in both datasets using sagittal slices show that the datasets are not aligned with each other. We explored two slices positioned at the left and right ventricles. The right side of the Corpus Callosum shows more differences than the left side. This might indicate a rotation around the anteroposterior axis between acquisition of both datasets.

We also observed a motion artifact at the forceps major. This artifact is shown in figure 5.2.

The image shows colored spheres using the ADC where a line of yellow colored spheres can be seen. This line follows the Forceps Major which indicates a motion artifact.

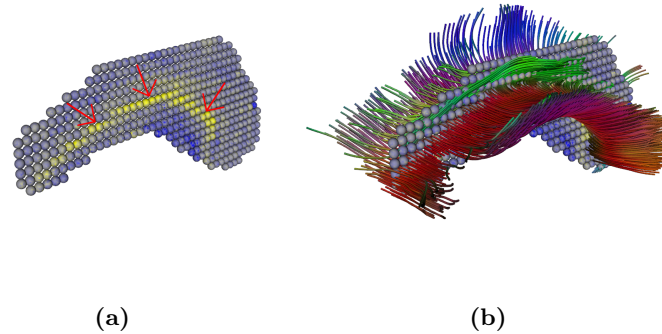


**Figure 5.1:** Corpus Callosum showing motion artifact. (a) shows colored spheres glyphs (using ADC) and (b) shows anatomical context with reconstructed fiber tracts from the first tensor dataset. The motion artifact showing glyphs with increased ADC is annotated with yellow arrows.

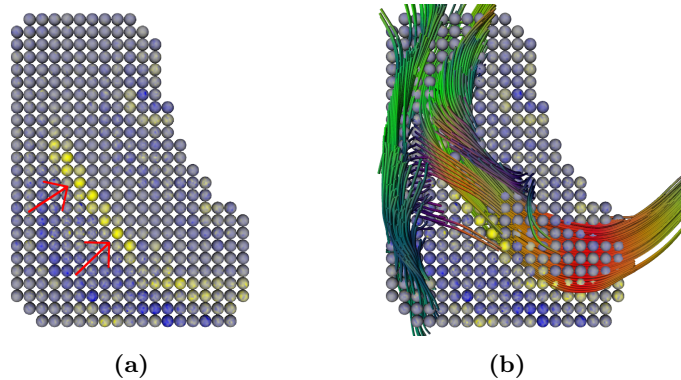


**Figure 5.2:** Motion artifact in forceps major. (a) shows colored spheres glyphs (using ADC) and (b) shows anatomical context with reconstructed fiber tracts from the first tensor dataset. The motion artifact showing glyphs with increased signal is annotated with yellow arrows.

### Random noise

Random noise is observed in most areas of the dataset. Figure 5.3 shows an example of random noise in the Corpus Callosum area.

The colored spheres representation (figure 5.3 (b)) shows several directions which indicate large differences between both datasets. These are the blue and yellow dots on the spheres.

Figure 5.3 (a) shows the colored spheres with the reconstructed fiber tracts from the Corpus Callosum. Figure 5.3 (b) shows the colored spheres using the ADC. The Corpus Callosum is an area which is linearly anisotropic. Large difference therefore do not coincide with expectations for this region. It can also be seen from the image that the large difference peaks often appear in co-linear direction to the fiber orientation (left to right in figure 5.3 (b)). This indicates a higher susceptibility to noise for the direction of the fiber tracts.

Figure 5.4 shows a single voxel in the Corpus Callosum area. Though the

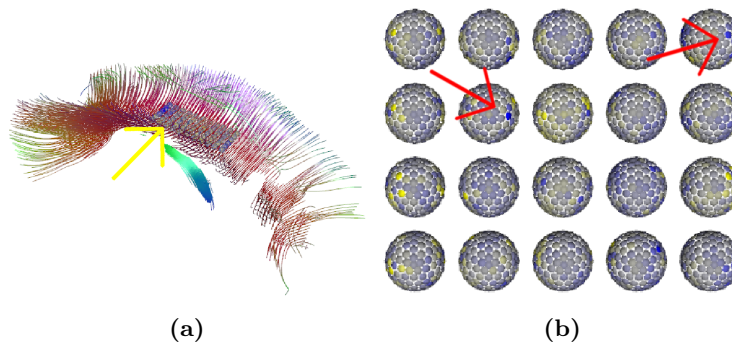


**Figure 5.3:** Random noise in the Corpus Callosum area. (a) shows the context of the ROI with reconstructed fiber tracts to represent the Corpus Callosum. (b) shows the ROI. Red arrows show examples of random noise.

voxel is linearly anisotropic in both datasets, larger differences can be seen in some of the measured directions.

#### Inhomogeneous $B_0$ field

Figure 5.5 shows an artifact at the anterior side of the brain (bottom of image). Unexpected features can be seen at the anterior of the brain on the axial view in figure 5.5 (a). Figure 5.5 (b) shows a sagittal view of the artifact.

This artifact is visible in slices 10 through 16 of the dataset. The artifact is caused by tissue/air boundaries around air cavities in the frontal area of the head.

#### White matter boundary

Large deviations between both datasets can be observed at the boundary of the white matter. This is shown in figure 5.5 (a) and figure 5.6.

The boundary does not consist of white matter. Therefore the measured data represents other tissue which does not reflect any relevant diffusion data. Both normalized signal attenuation difference and normalized ADC difference metrics show the boundary more obvious than the non-normalized difference metrics. This is caused by significantly smaller values inside the boundary region than values inside the white matter.

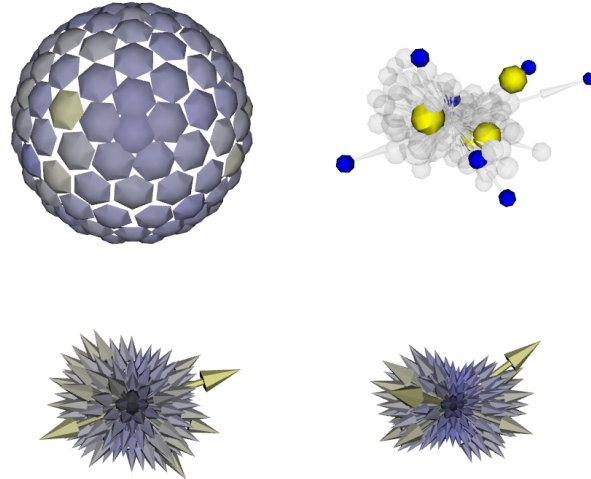


**Figure 5.4:** Random noise in single voxel in the Corpus Callosum area. The top row images show difference in ADC (partial spheres and projected arrows representation). The bottom row shows arrows representation from the first and second dataset (both normalized to the dataset).

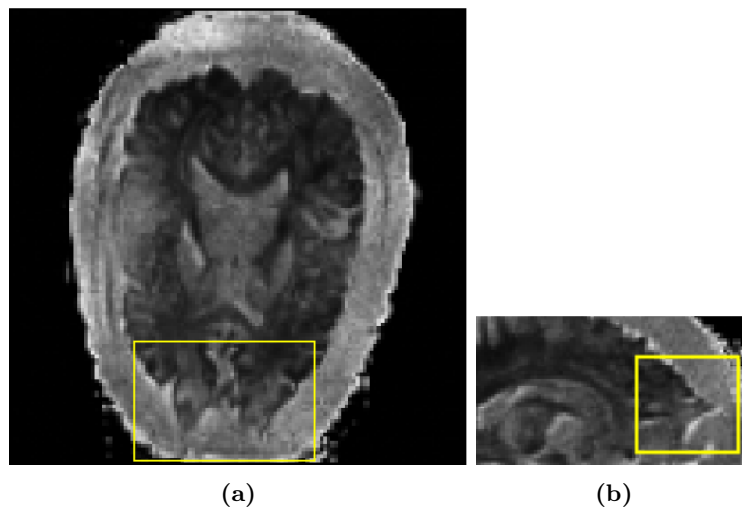


**Figure 5.5:** Artifact due to air cavities in the frontal area of the brain. (a) shows axial view and (b) shows sagittal view of the artifact, annotated with a yellow square.

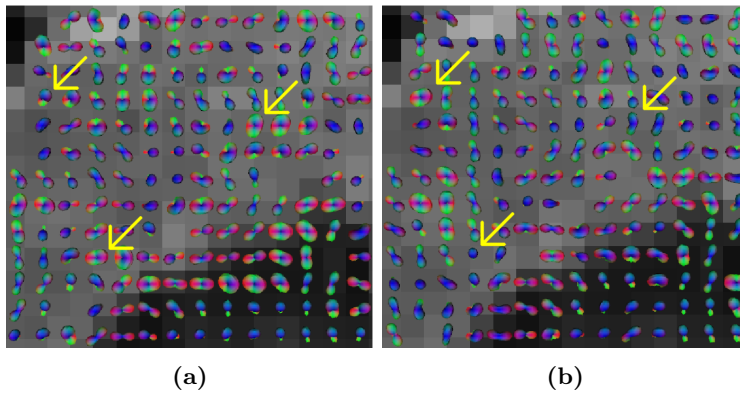


**Figure 5.6:** Noise at the boundary of the white matter. (a) and (b) show both datasets with Q-ball reconstructed glyphs representations. The arrows annotate several examples of voxels which appear to show a random difference in this area of the dataset.

## Chapter 5. Results

## 6.1 Conclusion

We developed techniques for the direct and comparative visualization of HARDI data integrated in a visualization framework. We present new glyph representations and techniques to compute, visualize and explore differences between two HARDI datasets.

We were able to create a complete conversion pipeline for PAR/REC data from the scanner to be converted to native DTITool format for visualization. Our glyph representations for the direct visualization of HARDI visualize the signal attenuation or the ADC derived from the signal attenuation. This representation of HARDI data is positively received by expert MRI physicists. The representations offer a new way to represent DWI data which allows for detailed exploration of HARDI data.

We developed a complete comparative visualization pipeline for the exploration of differences between two HARDI datasets. First we defined six difference metrics to represent the difference between two voxels as a scalar value. The PCA/FA difference metric provides a first step for a more advanced difference metric based on the FA as well as anisotropy measures. Then ROI selection allows for zooming into the data for individual voxel exploration. We developed three glyph representations specific to comparative visualization which display directional dependent differences for each voxel.

For rapid exploration of the HARDI data, we developed a multiple linked views layout including a 3D cursor for spatial reference. Different glyph representations can be explored at the same time. A context view is provided to relate local differences on a global scale. The 3D cursor allows for spatial reference in the visualization and for gradient direction selection using our glyph representations. This selection is linked to the slice viewer for gradient direction slice view exploration.

Our visualization techniques integrated in a visualization framework proves to be effective for the direct and comparative visualization of HARDI data. Several techniques were received well whereas others can be refined or extended to be more effective. Based on the case study, informal discussions and our own

analysis, we have identified future research topics for improvement of techniques and for global research directions. These will be discussed in section 6.3.

## 6.2 Discussion

### direct HARDI glyphs

Our glyph representations provide a novel exploration method for HARDI data. The effectiveness of the representations is however limited by visual complexity, occlusion and ambiguity of the glyph representations. Each glyph consists of 162 gradient directions which results in 162 individual features for a single glyph. The visual complexity is partially reduced by higher level glyph shapes like the spheres representation or the power crust surface representation.

The cones, cubes and dots representations are sometimes ambiguous due to the undefined origin of the glyph. For 3D perception of the glyph, often more interaction (i.e. rotation) is required. Occlusion is decreased however as the signal values are located at the outer edge of the glyph.

Occlusion occurs with representations like the spheres or projected arrows where part of the glyph is not seen. As became clear during informal discussions, some hidden parts might be significant to the understanding of the data. We partially solved this problem by adding color scales which include transparency, and by allowing interactive modification of the color scale range. This increases visibility of significant values.

### comparative HARDI glyphs

Results from the case study showed that performance was an issue for showing directional dependent data using glyphs for comparative visualization. In an attempt to improve on this issue we developed the partial and colored sphered representations. The projected arrows representation is best to visualize directional dependent data. The colored spheres representation can however be used to explore full slice differences due to its simple geometrical shape. The colored spheres representation was well received at a meeting after the case study.

We also used a VTK native Level Of Detail (LOD) actor within DTITool in an effort to increase performance. It showed that implementing a LOD system for the glyphs greatly improves performance when displaying large quantities of glyphs at the same time. There were however issues using the actor where certain features of the multiple views layout did not function correctly. Also normals were not respected where the models were sometimes appearing different than initially designed when the user interacts with the visualization.

### Color scale and transparency

Ordering of the polygons is an issue when using transparency for the glyphs. The polygons of the glyph are not depth-ordered which results in overlapping of polygons (figure 6.1 (a)). This problem is more prominent with 3D ROIs such as the fiber tract seeding.

We have experimented with two algorithms to sort the polygons. The first is to use depth peeling. This technique introduces multiple rendering passes which makes this algorithm computationally expensive. The complexity of the

glyphs requires a large number of rendering passes. When the number of passes was set to a level which resulted in a significantly improved visualization, the performance was decreased to unacceptable frame rates for interactive visualizations.

For the second technique we used the `vtkDepthSortPolyData` class (figure 6.1 (b)). This technique improved results for the glyphs where depth-sorting artifacts were resolved. These improvements were however relatively limited compared to the performance which also significantly decreased with this technique.

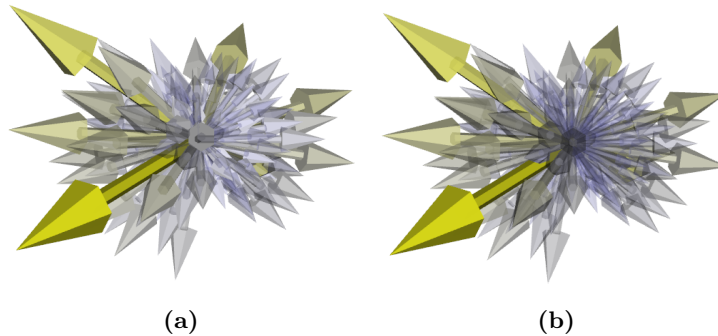


**Figure 6.1:** Depth sort with transparent glyphs. (a) shows no depth sorting while (b) uses the `vtkDepthSortPolyData` class to sort the polygons prior to rendering.

### difference metrics

The developed volume visualization of the difference metrics was well received during the case study. Global difference visualization allowed the user to quickly get affinity with the data. With the discussion during and after the case study, it showed that the difference metric was an important subject. In an effort to improve on the difference metrics we presented a conceptual design of the PCA/FA difference metric. Combination of anisotropy measures and the FA is a first attempt for a metric representing the difference between two voxels for specific research questions.

With our implementation of the conceptual PCA/FA difference metric, one of the difficulties encountered was definition of the thresholds. The thresholds for FA and  $c_l$  for example were empirically chosen. Determining the variables is also subject to characteristics of the data being visualized. In the ideal situation, the user should be allowed to interactively change these parameters for the most effective visualization. Too many degrees of freedom however might limit the user to create effective visualizations due to time constraints for definition of the thresholds. During a meeting, a suggestion was given to provide the user with several options of pre-defined 'good' parameters.

### 6.3 Future work

This section discusses several future research topics for the direct and comparative visualization of HARDI data.

### **Improved difference metric**

Our conceptual design of the PCA/FA difference metric can improve identification of areas of interest. The current implementation shows that the main concern is the determination of 'good' parameters for the metric.

This problem can be solved in two ways. The first allows the user to specify these parameters with intuitive GUI components. Two graphs are then included. The first graph allows for the specification of the different parts of the difference metric. The other graph can then be used to assign color ranges to these difference values. It should be possible to create discrete functions for the color graph. This allows each part of the difference metric to be presented with a different color instead of a color gradient.

A second method is to select some parameter sets. Each set should then be set to display a particular feature of the difference. For example, the parameters could be tuned to display the difference in linear anisotropy. The user is then presented with a collection of sets of parameters.

### **Slice view visualization**

The slice view is a simple yet powerful method to visualize global data. The slice view does however interfere sometimes with the visualization where it occludes the glyphs. As the glyphs are rendered at the surface, half of the glyph is usually rendered behind the slice view.

One of the solutions is to allow the user to set a transparency level for the slice view. With minimum opacity, the slice view provides context while not interfering with the visualization. Another method is to remove the slice view and project colors from the slice view on the glyphs. This however replaces the signal intensity color scale used for the glyphs.

The 3D slice viewer should also have support for 3D ROI drawing. Provided that the 3D slice viewer can be configured to display all relevant metrics, the 2D slice viewer could be removed from the visualization.

### **Conversion pipeline**

The conversion pipeline now consists of two different software packages and has a number of steps. DTITool is scheduled to have NIfTI-1 support in the near future. Some of these steps will then be deprecated and the pipeline will be shorter.

A second option to reduce the number of steps is to build a reader in DTITool for the PAR/REC format. No conversion tools will be necessary then. DTITool however now employs different readers for DTI and HARDI data. The reader can be designed to either have a tensor and HARDI dataset or only a HARDI dataset. The latter requires the application to be migrated to derive all data from the HARDI dataset.

### **2D glyph representation**

Occlusion is one of the main problems with various glyph representations. Also performance can be improved when visualizing large numbers of glyphs. Both issues can be improved on by making use of 2D glyphs.

Implementing a 2D representation for each voxel improved performance because of the absence of complex geometrical models. The representation however is more abstract. A procedural texture can be used on the 2D surface which represents the gradient directions, eigenvectors, voxel classification or other data derived from the HARDI data. This more abstract representation can be used to visualize trends in the data. These trends are visible by returning patterns over multiple 2D glyphs. An overview of several pixel-oriented visualization techniques are discussed in a paper by Keim in 2000 [Kei00]. The paper discussed issues with high importance and provides a formal basis for pixel-oriented visualization techniques.

### **Details-on-demand**

Zooming in with details on demand can increase effectiveness of the visualization. We propose a details-on-demand system where details are gradually added to the scene when the user zooms in.

The following could be an example of such a system. First, the slice view or volume visualization is shown. When the user identifies an area of interest, glyphs are being rendered at a certain zoom level showing directional dependent differences. This can be the colored spheres representation for example. When even further zooming in, the representations change from less detailed like the colored spheres representation to a more detailed representation like the projected arrows.

During the zoom, the more global data can be made transparent to serve as context. This preserves the context and provides gradual changes from global to local zoom level.

The lower resolution glyphs mentioned above can be used in combination with this item as well. For example, the slice view showing the difference metric can be gradually changed to 2D glyphs for each voxel showing directional dependent difference data. With experimental use of a native LOD actor showing mixed results, a custom LOD actor can possibly be used to obtain best results for combined details-on-demand and LOD system.

### **White matter mask**

One of the problems encountered with the difference metrics is the large differences at the edge of the white matter. This poses problems with 3D volume visualization.

The use of a white matter mask can improve the visualization. This can be implemented by either creating a mask with an external application or with an algorithm in the DTITool. The normalized signal attenuation and normalized ADC difference metrics clearly show the boundary of the white matter. This knowledge can be used to define a custom white matter mask.

### **ROI size indication**

The size of the ROI is of importance for the representation chosen. Some require significant processing time to be created which delays the exploration of data. Annotating the selected ROI prior to rendering can improve effectiveness. The

user can first determine the optimal ROI selection before rendering. The annotation can contain the number of glyphs to be rendered or possibly an indication of the total rendering time.

### Store visualization parameters

Finding data of interest can be time consuming with large datasets. A range of different visualization techniques suits different research questions. When the visualization parameters can be saved for all four views, the user can quickly load these and continue data exploration. This decreases time to setup the correct visualization parameters for specific research questions.

### Anatomical context

Tractography techniques are now used to create sets of fiber tracts from the tensor dataset to provide anatomical context. However, only one of the datasets can be used for fiber tract generation as only one tensor set can be loaded.

Tractography can be improved by generating fiber tracts for both datasets. This provides anatomical context for both datasets. Also this allows comparison of fiber tracts from both datasets which can be used to study differences between the datasets. Using the HARDI data for fiber tract generation could prove useful in reducing the amount of data needed. Figure 6.2 shows an example of data using fiber tracts from both tensor datasets.

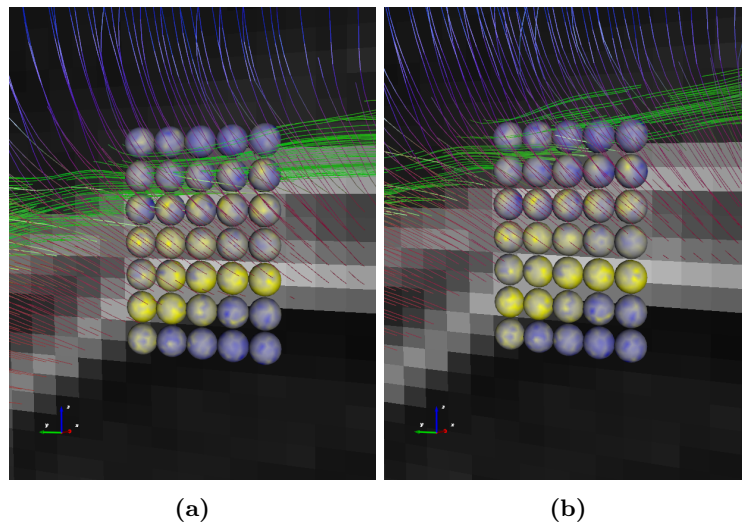


**Figure 6.2:** Fiber tracts from two tensor sets. (a) and (b) show fiber tracts from two different tensor datasets providing anatomical context for the same difference data visualized using the colored spheres representation.

### Difference transformation classification

The difference between two voxels can be considered a data transformation between these two voxels. These transformations can be classified. When a voxel is linearly anisotropic (high  $c_l$ ) for instance, a 90 degree rotation of the

principal fiber direction induces a specific difference pattern of the voxel. An example of such a pattern is shown in figure 6.3.

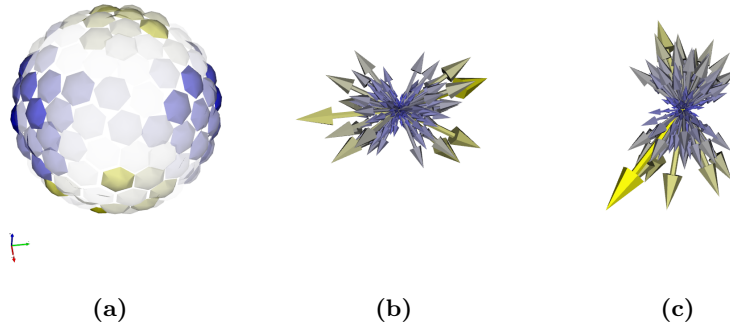


**Figure 6.3:** Classification pattern of a 90 degree rotation for a linearly anisotropic voxel. (a) shows the difference with increase of ADC at the top and bottom and decrease of ADC at the left and right side. (b) and (c) show the original two datasets using the arrows representation.

Classification of these difference transformations can be used for quick identification of differences of interest. Specifying boundaries for these classes can enable (semi-)automatic classification. When selecting a voxel for example, neighboring voxels can be selected automatic based on the difference transformation class of the selected voxel.

## Chapter 6. Conclusion

# APPENDIX A

---

## RECONSTRUCTION METHODS

This appendix gives a more detailed introduction to the mathematical background of DWI data. Several commonly used reconstruction methods are briefly explained.

### A.1 Processing the signal

#### A.1.1 Acquisition

The signal from a MRI scanner is usually 4-dimensional. The data space is described by a 3D volume of voxels. For each voxel information is gathered describing its diffusion properties. The diffusion is measured in a number of gradient directions which is the fourth dimension of the data. Along with these gradient directions, one or more images are unweighted meaning that no diffusion is measured. These images have a 0 gradient and are referred to as the  $B_0$  images. The  $B_0$  images are used in several equations and are used as reference for the weighted images.

The process of diffusion can be modeled using Fick's law of diffusion:

$$\frac{\partial}{\partial t}P(\mathbf{r}, t) = D\nabla^2P(\mathbf{r}, t) \quad (\text{A.1})$$

where  $D$  is the diffusion coefficient which depends on molecule type and medium properties.

For DWI, Stejskal and Tanner derived an equation which relates the signal to diffusion [ST65]. Using the assumption that the signal decay is exponential and the diffusion PDF is Gaussian, the relation is described with [Cal91, Bam03]:

$$S_i = S_0 e^{-bg^T D_i g} \quad (\text{A.2})$$

Here  $S_i$  is the measured signal (for the  $i$ -th gradient direction),  $S_0$  is the unweighted image where no gradient is applied,  $D_i$  is the Apparent Diffusion Coefficient (ADC) and  $b$  is the diffusion-sensitizing factor.  $b$  is defined as

$$b = \gamma^2 \delta^2 (\Delta - \delta/3) \quad (\text{A.3})$$

Here  $\gamma$  is the gyromagnetic ratio,  $\delta$  is the gradient pulse time and  $\Delta$  is the delay of the gradient pulse.

The sensitivity of the scan is defined by the  $b$ -value. Increasing this value gets more sensitive results but a number too high results in unwanted artifacts in the image. Several studies searched for optimal acquisition schemes for HARDI acquisition [PRP<sup>+</sup>08].

### A.1.2 Relating signal to diffusion

The signal from the MRI scanner can be modeled in a (3D) diffusion Probability Distribution Function (PDF). It is also known as Probability Density Function or Diffusion Function. It describes the probability of a water molecule's displacement in a certain direction. The relation between the measured signal and the PDF is described by a 3D Fourier transform [OSV<sup>+</sup>06, Cal91]:

$$P(\mathbf{R}) = \int E(\mathbf{q}) \exp(-2\pi i \mathbf{q} \cdot \mathbf{R}) d\mathbf{q} \quad (\text{A.4})$$

with  $\mathbf{q}$  the space vector and  $\mathbf{R}$  the displacement defined by  $q = \gamma\delta G/2\pi$  with  $\gamma$  the gyromagnetic ratio and  $\delta$  and  $G$  respectively being the duration and sensitivity of the diffusion gradient vector. The resulting function describes the 3D probability space. Several ways can be used to reduce this space for practical application. One of these is transformation to the ODF which is described in the next section.

### A.1.3 ODF

The PDF is a probability function which can be modeled in a Orientation Distribution Function (ODF). This ODF is in fact a radial projection of the PDF and gives a distribution over a sphere. It is defined as

$$\psi(\mathbf{u}) = \frac{1}{Z} \int_0^\infty P(r\mathbf{u}) dr \quad (\text{A.5})$$

Where  $Z$  is a dimensionless normalization constant.

The ODF describes the diffusion in a certain direction. When the ODF is min/max normalized, the spikes give the general direction of diffusion. These are two spikes for linear anisotropy or more for planar or spherical anisotropy.

## A.2 Spherical Harmonics

Spherical harmonics (SH) are the angular portion of a set of solutions to Laplace's equation. They form an orthogonal system for arbitrary spherical function  $f(\theta, \phi)$  which is expressed by the Laplace series[Weia]

$$f(\theta, \phi) = \sum_{l=0}^{\infty} \sum_{m=-l}^l a_l^m Y_l^m(\theta, \phi) \quad (\text{A.6})$$

The SH are expressed in spherical coordinates[Weib] and are explicitly defined via associated Legendre polynomials  $P_l^m$

$$Y_l^m(\theta, \phi) = N P_l^m(\cos \theta) e^{i m \phi} \quad (\text{A.7})$$

where  $N$  is a normalization term and is defined as

$$N = \sqrt{\frac{2l+1}{4\pi} \frac{(l-m)!}{(l+m)!}} \quad (\text{A.8})$$

SH are used to represent the ODF reconstructed using one of the reconstruction methods. The SH allows for specification of a number of coefficients. These coefficients can then be used to deform a sphere to reflect the diffusion profile of a voxel.

### A.3 Reconstructing the PDF

Several ways have been proposed to reconstruct the PDF from the measured signal. This section will explain some of the basics of Diffusion Spectrum Imaging (DSI) [WRT<sup>+</sup>00], Q-ball imaging [Tuc04], Spherical Deconvolution [TCGC04] and the Diffusion Orientation Transform (DOT) [OSV<sup>+</sup>06].

#### Diffusion Spectrum Imaging

One of the most straightforward ways of generating the PDF is by inverse 3D Fourier Transformation (3DFT) of the measured signal. This process has been described by [WRT<sup>+</sup>00] and was referred to as Diffusion Spectrum Imaging (DSI). This relation between the signal and the transform has already been discussed and is given by Equation A.4.

#### Q-ball imaging

Q-ball imaging is a technique which utilizes the Funk-Radon transform (FRT). Consider a distribution over a sphere. Then the FRT is defined for a vector  $\mathbf{u}$  as the set of points perpendicular to that vector. This can be written as

$$\begin{aligned} \xi[f(\mathbf{w})](\mathbf{u}) &= \int_{\mathbf{w} \in \mathbf{u}^\perp} f(\mathbf{w}) d\mathbf{w} \\ &= \int f(\mathbf{w}) \delta(\mathbf{w}^T \mathbf{u}) d\mathbf{w} \end{aligned} \quad (\text{A.9})$$

where  $\delta$  is the Dirac delta function [Tuc04].

#### Spherical Deconvolution

Healy et al. introduced a paper in 1998 proposing the concept of Spherical Deconvolution [HHK98]. These principles were later used to create a new reconstruction method for DWI [TCGC04].

The measured signal attenuation can be described as the convolution of the ODF with the diffusion weighted signal. Then the ODF can be obtained using the spherical deconvolution technique described by [HHK98]. It should be noted that the fiber bundles are assumed to have identical diffusion characteristics. Deviations are assigned to partial volume effects.

Later on, several improvements were introduced based on the concept of Spherical Deconvolution. These include Constrained Spherical Deconvolution (CSD), Super-resolved Constrained Spherical Deconvolution (super-CSD) and Maximum-Entropy Spherical Deconvolution [Ale05, TCC07].

### **Diffusion Orientation Transform**

The Diffusion Orientation Transform (DOT) uses the Fourier transform between the measured signal and the probability expressed in spherical coordinates [OSV<sup>+</sup>06]. Two versions have been developed, a parametric one and a non-parametric one which utilizes the Legendre polynomials.

The signal is assumed to have exponential attenuation. Then the radial part of the Fourier integral is evaluated analytically. The resulting functions are evaluated at a fixed radius of a sphere. Spherical harmonics are then generated to describe the probabilities on a sphere with fixed radius. Also a non-parametric case is proposed which utilizes Legendre polynomials.

# APPENDIX B

---

## DTITool MOUSE AND KEY BINDINGS

Action	Mousebutton	keyboard
translate	middle button	
translate	left button	Shift
rotate (around focus point)	left button	
rotate (axial to camera)	left button	Ctrl
zoom	scrollwheel	
zoom	right button	
ROI drawing (2D view)	left button	

**Table B.1:** Mouse and keyboard combinations for moving the camera around in the visualization.

Key binding	Description
<b>Existing</b>	
w	Switch to wireframe rendering
s	Switch to solid rendering
f	Zoom and focus to current mouse position
Ctrl+o	Load tensor dataset
Ctrl+h	Load HARDI dataset with default HARDI reader
Ctrl+q	Quit DTITool
Ctrl+1	Change to All, large 3D layout
Ctrl+2	Change to All, same size layout
Ctrl+3	Change to 3D layout
Ctrl+4	Change to Sagittal (X) layout
Ctrl+5	Change to Coronal (Y) layout
Ctrl+6	Change to Axial (Z) layout
Ctrl+t	Show/hide option tabs
Ctrl+b	Background color
Ctrl+l	Color lookup tables
Ctrl+p	Make screenshot
Ctrl+f	Print FPS
Ctrl+m	Masking threshold
<b>Added</b>	
p	Place 3D cursor / Select gradient direction
Ctrl+7	Change to Multiview (4 3D) layout
Ctrl+Shift+1	Select view 1 as active
Ctrl+Shift+2	Select view 2 as active
Ctrl+Shift+3	Select view 3 as active
Ctrl+Shift+4	Select view 4 as active
1	Select dataset 1 for gradient slice view
2	Select dataset 2 for gradient slice view
Space	Reset view and focus on current visualization

**Table B.2:** Existing and added key bindings in DTITool.

# APPENDIX C

---

## EXPORT ROI FILE FORMAT

The export ROI function added to DTITool generates three files for each loaded dataset. These are the gradient, signal and voxel position files. A description and file format specification will now be discussed.

The *gradient* files contain three lines holding values for the X, Y and Z coordinates. The values are separated with spaces. The  $B_0$  gradient is also included. Next is an example of the format for the first part of the file:

```
0 1 0 0 -1 0 0 0 -0.955423 ...
0 0 1 0 0 -1 0 0.525731 0.155218 ...
0 0 0 1 0 0 -1 -0.850651 -0.251148 ...
```

These translate in the gradient direction vectors

$$\begin{bmatrix} 0 \\ 0 \\ 0 \end{bmatrix}, \begin{bmatrix} 1 \\ 0 \\ 0 \end{bmatrix}, \begin{bmatrix} 0 \\ 1 \\ 0 \end{bmatrix}, \begin{bmatrix} 0 \\ 0 \\ 1 \end{bmatrix}, \begin{bmatrix} -1 \\ 0 \\ 0 \end{bmatrix}, \begin{bmatrix} 0 \\ -1 \\ 0 \end{bmatrix}, \begin{bmatrix} 0 \\ 0 \\ -1 \end{bmatrix}, \begin{bmatrix} 0 \\ 0.525731 \\ -0.850651 \end{bmatrix}, \begin{bmatrix} -0.955423 \\ 0.155218 \\ -0.251148 \end{bmatrix}, \dots$$

For the *signal* files, each line represents a voxel. The order of the values correspond to the order of the gradient directions. The values are separated with spaces. An example for two glyphs is:

```
60 14 39 32 21 33 24 19 19 21 ...
73 16 24 22 20 32 22 15 23 21 ...
```

The *voxel position* files contain the grid at which the voxels are located. Each line in this file represents a coordinate for a voxel. The lines of the signal files and the voxel position files correspond with each other. An example for two glyphs is:

```
88 96 0
88 98 0
```

These two glyphs are situated at coordinates

$$\begin{bmatrix} 88 \\ 96 \\ 0 \end{bmatrix} \text{ and } \begin{bmatrix} 88 \\ 98 \\ 0 \end{bmatrix}$$

## Chapter C. Export ROI file format

Generated files can be used to load data in other software tools. The file format is supported by Matlab [Mat]. The command to load the data is:

```
load -ascii <filename>.dat
```

The file is then loaded in a variable with the name <filename>.

## BIBLIOGRAPHY

- [ACK01] Nina Amenta, Sunghee Choi, and Ravi Krishna Kolluri. The power crust. In *SMA '01: Proceedings of the sixth ACM symposium on Solid modeling and applications*, pages 249–266, New York, NY, USA, 2001. ACM.
- [Ale05] Daniel C. Alexander. Maximum entropy spherical deconvolution for diffusion MRI. In Gary E. Christensen and Milan Sonka, editors, *IPMI*, volume 3565 of *Lecture Notes in Computer Science*, pages 76–87. Springer, 2005.
- [APBG01] D.C. Alexander, C. Pierpaoli, P.J. Basser, and J.C. Gee. Spatial transformations of diffusion tensor magnetic resonance images. *Medical Imaging, IEEE Transactions on*, 20(11):1131–1139, nov. 2001.
- [Bam03] Roland Bammer. Basic principles of diffusion-weighted imaging. *European Journal of Radiology*, 45(3):169–184, 2003.
- [Cal91] P. Callaghan. *Principles of Nuclear Magnetic Resonance Microscopy*. 1991.
- [CVCM09] Guang Cheng, Baba C. Vemuri, Paul R. Carney, and Thomas H. Mareci. Non-rigid registration of high angular resolution diffusion images represented by gaussian mixture fields. In *MICCAI '09: Proceedings of the 12th International Conference on Medical Image Computing and Computer-Assisted Intervention*, pages 190–197, Berlin, Heidelberg, 2009. Springer-Verlag.
- [HHK98] Dennis M. Healy, Jr., Harrie Hendriks, and Peter T. Kim. Spherical deconvolution. *J. Multivar. Anal.*, 67(1):1–22, 1998.
- [HJM<sup>+</sup>06] P. Hagmann, L. Jonasson, P. Maeder, J. Thiran, V. Wedeen, and R. Meuli. Understanding Diffusion MR Imaging Techniques: From Scalar Diffusion-weighted Imaging to Diffusion Tensor Imaging and Beyond. *Radiographics*, 26:S205–S223, 2006.

## BIBLIOGRAPHY

- [Hor96] Joseph Hornak. *The Basics of MRI*, volume 2010. Interactive Learning Software, Henrietta, NY, 1996.
- [Hut] Tim J. Hutton. A VTK port of the powercrust algorithm. <http://www.sq3.org.uk/powercrust/>.
- [Kei00] Daniel A. Keim. Designing pixel-oriented visualization techniques: Theory and applications. *IEEE Transactions on Visualization and Computer Graphics*, 6:59–78, 2000.
- [Kin04] Gordon Kindlmann. Superquadric tensor glyphs. In *Proceeding of The Joint Eurographics - IEEE TCVG Symposium on Visualization*, pages 147–154, May 2004.
- [KW99] Gordon Kindlmann and David Weinstein. Hue-balls and lit-tensors for direct volume rendering of diffusion tensor fields. In *VIS '99: Proceedings of the conference on Visualization '99*, pages 183–189, Los Alamitos, CA, USA, 1999. IEEE Computer Society Press.
- [KWW<sup>+</sup>05] L-W. Kuo, V. J. Wedeen, J-C. Weng, T. G. Reese, J-H. Chen, and W-Y. I. Tseng. Using track similarity to determine optimum sequence parameters for diffusion spectrum imaging. In *Proceedings of the 13th ISMRM Scientific Meeting & Exhibition*, page 391. International Society for Magnetic Resonance in Medicine, 2005.
- [Lev] Haim Levkowitz. Various perceptually linear color scales. <http://www.cs.uml.edu/~haim/ColorCenter/>.
- [LH92] Haim Levkowitz and Gabor T. Herman. Color scales for image data. *IEEE Computer Graphics and Applications*, 12:72–80, 1992.
- [Mat] Matlab by mathworks. <http://www.mathworks.com/>.
- [May] The ANALYZE data format. [http://cancercenter.mayo.edu/mayo/research/robb\\_lab/analyze.cfm](http://cancercenter.mayo.edu/mayo/research/robb_lab/analyze.cfm).
- [Med] The DICOM standard. <http://medical.nema.org/>.
- [Mun09] Tamara Munzner. *Fundamentals of Computer Graphics*, chapter 27, pages 675–707. A K Peters, 3. edition, 2009.
- [Neu] The NIfTI-1 data format. <http://nifti.nimh.nih.gov/nifti-1>.
- [OSV<sup>+</sup>06] Evren Özarlan, Timothy M. Shepherd, Baba C. Vemuri, Stephen J. Blackband, and Thomas H. Mareci. Resolution of complex tissue microarchitecture using the diffusion orientation transform (DOT). *NeuroImage*, 31(3):1086 – 1103, 2006.
- [Poo05] Robert A. Pooley. Fundamental physics of MR imaging. *Radio-Graphics*, 25(4):1087–1099, July 2005.

## BIBLIOGRAPHY

- [PPvA<sup>+</sup>09] T. H. J. M. Peeters, V. Prckovska, M. van Almsick, A. Vilanova, and B. M. ter Haar Romeny. Fast and sleek glyph rendering for interactive HARDI data exploration. In *PACIFICVIS '09: Proceedings of the 2009 IEEE Pacific Visualization Symposium*, pages 153–160, Washington, DC, USA, 2009. IEEE Computer Society.
- [PRP<sup>+</sup>08] Vesna Prčkovska, Alard F. Roebroek, W. L. Pullens, Anna Vilanova, and Bart M. Haar Romeny. Optimal acquisition schemes in high angular resolution diffusion weighted imaging. In *MICCAI '08: Proceedings of the 11th International Conference on Medical Image Computing and Computer-Assisted Intervention, Part II*, pages 9–17, Berlin, Heidelberg, 2008. Springer-Verlag.
- [Smi02] Lindsay I. Smith. A tutorial on principal components analysis, 2002.
- [ST65] E. O. Stejskal and J. E. Tanner. Spin diffusion measurements: Spin echoes in the presence of a time-dependent field gradient. *The Journal of Chemical Physics*, 42(1):288–292, 1965.
- [TCC07] J-Donald D. Tournier, Fernando Calamante, and Alan Connelly. Robust determination of the fibre orientation distribution in diffusion MRI: non-negativity constrained super-resolved spherical deconvolution. *NeuroImage*, 35(4):1459–1472, May 2007.
- [TCGC04] J-Donald D. Tournier, Fernando Calamante, David G. Gadian, and Alan Connelly. Direct estimation of the fiber orientation density function from diffusion-weighted MRI data using spherical deconvolution. *NeuroImage*, 23(3):1176–1185, November 2004.
- [TRW03] D. Tuch, T. Reese, and M. Wiegell. Diffusion MRI of complex neural architecture. *Neuron*, 40(5):885–895, December 2003.
- [Tuc04] David S. Tuch. Q-ball imaging. *Magnetic Resonance in Medicine*, 52(6):1358–1372, 2004.
- [TWBW99] D. S. Tuch, R. M. Weisskoff, J. W. Belliveau, and V. J. Wedeen. High angular resolution diffusion imaging of the human brain. In *Proceedings of the 7th Annual Meeting of ISMRM*, page 321, 1999.
- [Weia] Eric W. Weisstein. "laplace series." from mathworld—a wolfram web resource. <http://mathworld.wolfram.com/LaplaceSeries.html>.
- [Weib] Eric W. Weisstein. "spherical harmonic." from mathworld—a wolfram web resource. <http://mathworld.wolfram.com/SphericalHarmonic.html>.
- [WKM08] Dominik Weishaupt, Victor D. Kchli, and Borut Marincek. *How Does MRI Work?* Springer-Verlag Berlin Heidelberg, 2 edition, 2008.
- [WPG<sup>+</sup>97] C.-F. Westin, S. Peled, H. Gudbjartsson, R. Kikinis, and F. A. Jolesz. Geometrical diffusion measures for MRI from tensor basis analysis. In *ISMRM '97*, page 1742, Vancouver Canada, April 1997.

## BIBLIOGRAPHY

- [WRT<sup>+</sup>00] V.J. Wedeen, T.G. Reese, D.S. Tuch, M.R. Weigel, J.-G. Dou, R.M. Weiskoff, and D. Chessler. Mapping fiber orientation spectra in cerebral white matter with fourier transform diffusion mri. In *In Proc. of the 8th Annual Meeting of ISMRM*, page 82, 2000.
- [Yin08] Robert K. Yin. *Case Study Research: Design and Methods (Applied Social Research Methods)*. Sage Publications, Inc, 4th edition, October 2008.

- ADC** Apparent Diffusion Coefficient. 2, 9, 14, 16, 19, 20, 22, 47, 49
- CSD** Constrained Spherical Deconvolution. 65
- DOT** Diffusion Orientation Transform. 65, 66
- DSI** Diffusion Spectrum Imaging. 65
- DTI** Diffusion Tensor Imaging. 1, 9, 10
- DWI** Diffusion Weighted Imaging. 1, 5, 7, 31
- FA** Fractional Anisotropy. 10, 37, 46, 57
- fMRI** functional Magnetic Resonance Imaging. 31
- FOV** Field Of View. 49
- FRT** Funk-Radon transform. 65
- GUI** Graphical User Interface. 35, 38
- HARDI** High Angular Resolution Diffusion Imaging. 1, 10, 11, 13, 20, 32, 55
- LOD** Level Of Detail. 56
- MRI** Magnetic Resonance Imaging. 1, 5, 55
- ODF** Orientation Distribution Function. 9, 14, 16, 64
- PCA** Principle Component Analysis. 11, 15, 20, 23
- PDF** Probability Density Function. 8, 64
- RF** Radio Frequency. 5, 6
- ROI** Region Of Interest. 15, 18, 20, 37, 40, 44, 55, 59
- super-CSD** Super-resolved Constrained Spherical Deconvolution. 65